



HAL
open science

Steady vs. Dynamic Contributions of Different Doped Conducting Polymers in the Principal Components of an Electronic Nose's Response

Wiem Haj Ammar, Aicha Boujnah, Aimen Boubaker, Adel Kalboussi, Kamal Lmimouni, Sébastien Pecqueur

► To cite this version:

Wiem Haj Ammar, Aicha Boujnah, Aimen Boubaker, Adel Kalboussi, Kamal Lmimouni, et al.. Steady vs. Dynamic Contributions of Different Doped Conducting Polymers in the Principal Components of an Electronic Nose's Response. Eng, 2023, 4 (4), pp.2483-2496. 10.3390/eng4040141 . hal-04212911

HAL Id: hal-04212911

<https://hal.science/hal-04212911v1>

Submitted on 20 Sep 2023

HAL is a multi-disciplinary open access archive for the deposit and dissemination of scientific research documents, whether they are published or not. The documents may come from teaching and research institutions in France or abroad, or from public or private research centers.

L'archive ouverte pluridisciplinaire **HAL**, est destinée au dépôt et à la diffusion de documents scientifiques de niveau recherche, publiés ou non, émanant des établissements d'enseignement et de recherche français ou étrangers, des laboratoires publics ou privés.



Distributed under a Creative Commons Attribution 4.0 International License

Steady vs. Dynamic Contributions of Different Doped Conducting Polymers in the Principal Components of an Electronic Nose's Response

Wiem Haj Ammar^a, Aicha Boujnah^a, Aimen Boubaker^a, Adel Kalboussi^a, Kamal Lmimouni^b & Sébastien Pecqueur^{b*},

^a Department of Physics, University of Monastir Tunisia.

^b Univ. Lille, CNRS, Centrale Lille, Univ. Polytechnique Hauts-de-France, UMR 8520 - IEMN, F-59000 Lille, France.

Email: sebastien.pecqueur@iemn.fr

Abstract

Multivariate data analysis and machine-learning classification become popular tools to extract features without physical models for complex environments recognition. For electronic noses, time sampling over multiple sensing elements must be a fair compromise between a period sufficiently long to output a meaningful information pattern, and sufficiently short to minimize training time for practical applications. Particularly when reactivity's kinetic differs from thermodynamic in sensitive materials, finding the best compromise to get the most from data is not obvious. Here, we investigate on the influence of data acquisition to improve or alter data clustering for molecular recognition on a conducting polymer electronic nose. We found out that waiting for sensing elements to reach their steady state is not required for classification, and that reducing data acquisition down to the first dynamical information suffice to recognize molecular gases by principal component analysis with the same materials. Especially for online inference, this study shows that a good sensing array is no array of good sensors, and that new figure-of-merits shall be defined for sensing hardware aiming machine-learning pattern-recognition rather than metrology.

Keywords: conducting polymer, electronic nose, feature extraction, principal component analysis, molecular recognition

Introduction

Current advances in artificial intelligence and internet-of-things push identifying new input layers as data generators to feed machine-learning (ML) for information classification. Before this, electronic noses (eNoses) have nourished the fantasy for more than 60 years of emulating a biological sense to perform classification tasks that sensors can barely make with molecular patterns.[1-5] It is therefore very appropriate to wonder whether conventional approaches to select sensing hardware are adapted to information processing requirements, with pattern recognition having more standards nowadays.

Chemistry is no trivial physics: it is no 1D-continuum nor spectrum, but volatile molecules compose a vast group of hundred billion countable objects.[6, 7] Therefore, measuring all of them simultaneously with restricted and well-chosen set of ultimately selective sensors is unrealistic. If such complexity suits better ML-supported recognition than quantification using metrological sensors, proposing clear sensing figure-of-merits (FoM) that guide technologists to identify the right sets of materials is still needed in such context.[8-11] The main difficulty in identifying those lies in the fact that smart sensing arrays do not involve physical models at the opposite of metrological sensors: ML is purely mathematically-driven, which does not help in identifying device physical features to generate qualitative data. Each output signal conditions individual components of an input data, but the quality of the output data itself relates to features that affects the performances of the classifier as a group of device properties. The relationship between the data transformation as a result and the physical properties of a chosen sensing hardware is not straightforward and largely depends on the association of a software classifier with a sensing hardware. For an eNose, conductometric sensing arrays are often used as a hardware,[12-15] in conjunction with principal component analysis (PCA)/k-means clustering (k-means) as a classifier [5, 16-18]. In such systems, time-dependent current signals are inputted by environmentally sensitive materials in an array. Each current signal composes the feature of one single

coordinate of a high-dimensional vector for classification. PCA is a linear classifier as it involves only one matrix transformation from a dataset of input vectors to a set of scores. The PCA projects data on a subspace defined by a basis of the covariance-matrix eigenvectors which have the highest eigenvalues. As a consequence, PCA aims in ignoring the contributions of “silent” sensing elements, or the ones which activities that are uncorrelated to one another. Conventional sensors’ FoM do not consider information correlation between sensing elements, as it relates strictly to physical properties of individual elements to be standalone: for instance selectivity, sensitivity or time response.[19] The latter is an important FoM that usually defines if a technology is suitable for online application. If information speed is essential for telecommunication, it is not necessarily the case for the velocity of information carriers themselves. The implementation of recurrent networks for sensing elements can illustrate such fact, where the group dynamic of different slow sensing elements enables recognizing frequency-modulated signals.[20] Homogenizing the physical properties of the population of sensing elements can even yield to degrade the classifier recognition performances, so when the dynamic of sensing devices carries information, long-enough acquisition is crucial for classification.[20] However, time is also a resource to enrich a database to train a system: the slower the hardware the longer the training, which ultimately conditions any classifier’s recognition performance. As a consequence, in case information lies in the dynamic of a hardware,[21] a fair compromise must be found for data acquisition time to optimize training with enough meaningful data but reasonable training duration for environmental pattern recognition.

In the framework of recognizing volatile solvents with doped conducting polymers, we propose in this study to quantify how relevant is the acquisition time as metrological FoM for effective molecular recognition with a conductometric nose using PCA/k-means. By using both static and dynamic descriptors, we show that a steady sensing element response is unnecessary for optimal classification, and that training duration can greatly be shortened for practical inference.

Experimental Section

Device Fabrication: The fabrication of sensing elements used in this study has been reported elsewhere.[22] Concentric spiral-shaped Au microelectrodes (channel length $L = 400$ nm, spiral electrodes length W such as $W/L > 10^3$ in a round cavity of $28 \mu\text{m}$ in diameter) were micro-fabricated by electron beam lithography in a cleanroom environment. Devices active area features a large W/L over a restricted area to maximize conductance sensitivity while minimizing total area of an array of them for system integration. Contact lines are passivated by a conformal CVD-processed Parylene C passivation layer ($2 \mu\text{m}$ thickness), structured by an O_2 dry-etching to expose pads and devices active area, so each device outputs an individual response for co-integration at small scale. The active materials were subsequently deposited on top of the sensing arrays by drop casting. Formulations of regio-regular P3HT and dopants solutions (composed of $\text{Fe}(\text{OTf})_3$, $\text{Bi}(\text{OTf})_3$, $\text{Cu}(\text{OTf})_2$, $\text{In}(\text{OTf})_3$, $\text{Al}(\text{OTf})_3$, $\text{Dy}(\text{OTf})_3$ and $\text{Ce}(\text{OTf})_3$) were done in two different steps to minimize the device electrical property distribution due to material heterogeneity if deposited with a single formulation.

Electrical Characterization: As raw data, the study exploits current versus time measurements of eight populations of materials, composed of three different devices for each material. Each of the 24 current versus time trace sizes 6899 data points per current trace, sampled every second. The current measurements were done with an Agilent 4155 parameter analyzer in an air blow, passing through a 5-mL vial that contains 1 mL of a volatile solvent.[22] The system was calibrated to blow at a rate of 1 mL/s over a sensing array. The control of the vapor exposure was manually operated with pneumatic valves (asynchronous delays up to five seconds can be considered between the actual operation of the valves and the attributions of the labels on the current traces). Elementary sequences of gas exposures were set to three minutes for sensing elements to reach their steady-state. Each volatile solvent exposure is followed by a purging sequence, when the air flow passes through an empty vial, to let the response of the sensing arrays recover their response.

Data Analysis: Raw data currents were compiled and treated without filtering. Raw data curves have already been published,[**22**] and are available alongside on a public repository. Principal component analysis (PCA) was used as a linear classifier, by mean of the online open access tool Clustvis [**23**]. PCA data was scaled by unit variance and computed by singular value decomposition. All PCA data is available as supplementary information of this article. 95%-confidence ellipsoids were determined by k-means clustering with $k=3$, from random values for the initial centroids (in each case, k-means was run at least three times to ensure repeatability of the resulted clusters).

Results

Data Collection and Feature Extraction.

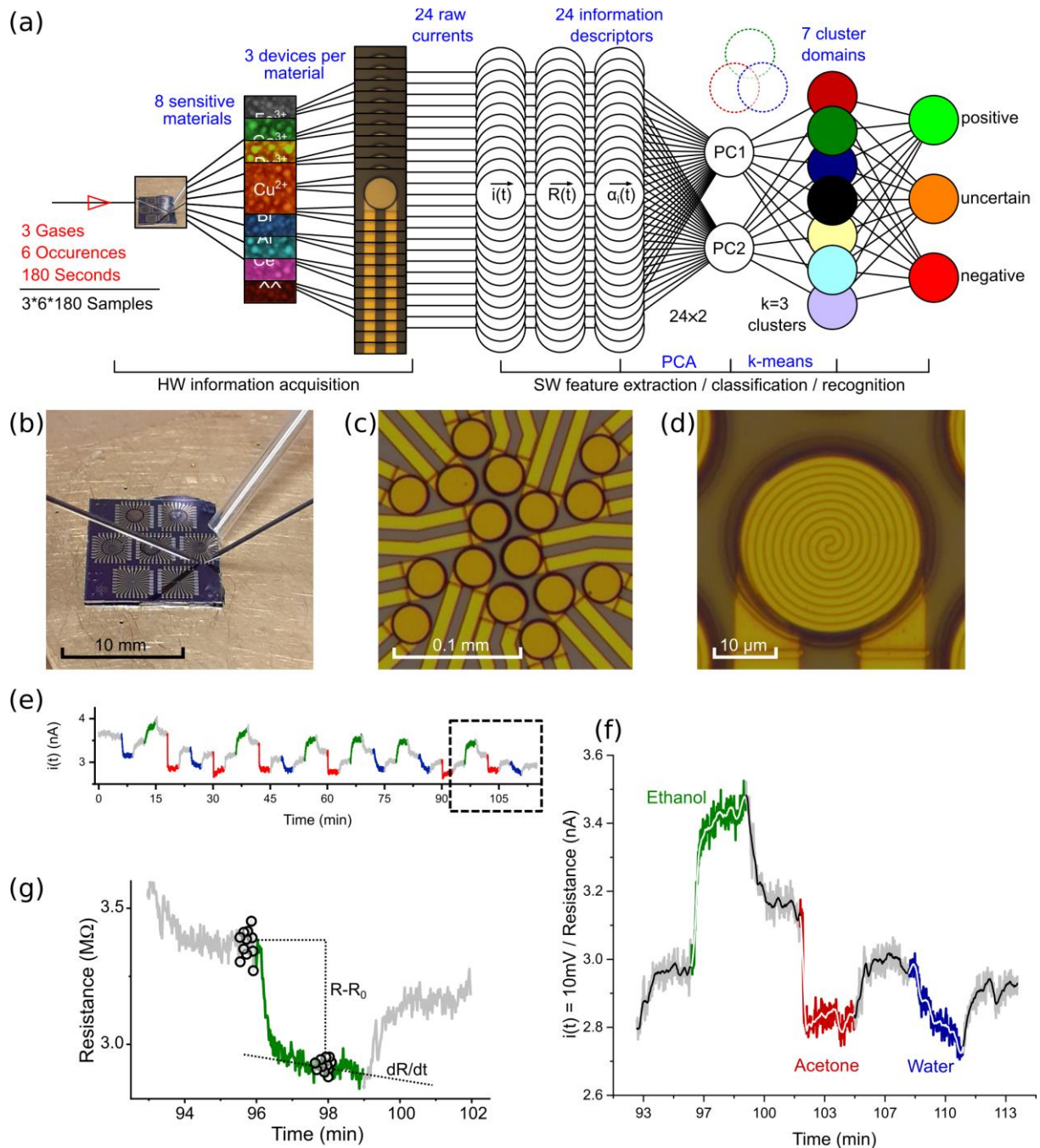


Figure 1. Classifier Structure for Solvent Vapor Recognition | a, Data classifier used in this study for unsupervised classification by using principal component analysis and k-means clustering on dynamical datasets generated by sensing elements composed of different materials. b-d, Pictures of the data acquisition hardware at different scales: photograph of seven arrays at the scale where each material were deposited (b), microscope picture of the active area of an array gathering 16 sensing elements (c), microscope picture of a single sensing element featuring a sub-micrometric conducting channel (d). e, Example of raw current signal output $i(t)$ from one single sensing element coated with one

specific material, exposed to different sequences of solvent vapor exposures. **f**, Zoom-in on one time sequence when three different vapors affect the sensing elements conductance between purge sequences (zoom-in on fig.1e trace marked by a dashed square window). **e-f**, Blue, green and red sequences depict the sensing element current output when water, acetone, ethanol vapors respectively are blown on the sensing elements with compressed air. Grey sequences depict the sensing element current output when clean compressed air is blown on the sensing elements. **g**, Resistance value $R(t)$ calculated from the raw current signal output $i(t)$. Parameters $R-R_0$ and dR/dt for calculating the information features $\alpha_1(t)$ and $\alpha_2(t)$ are depicted as the absolute resistance modulation and the slope of the resistance variation overtime, extrapolated from the values of ten resistance data points in each case.

To interpret the physical significance of information features for the quality of a recognition, the machine-learning (ML) approach is preferred to the deep-learning (DL) one (see Fig.1 for the overall approach). DL algorithms differentiate from ML ones mostly by their complexity to allow the end-user not to have to identify information descriptors from raw data *a priori*. In our case, we chose specifically to compare two different features α_1 and α_2 that are extensively used in conductometric eNoses as information descriptors: the relative resistance modulation $\alpha_1=R/R_0-1$ and the drift resistance $\alpha_2=\dot{R}/R$, with R the Ohmic resistance of a conductometric sensing element measured at a given time during the exposure to an environment of a specific class, \dot{R} its first derivative of time and R_0 its value right before it starts to be exposed to an environment of a specific class at t_0 . As α_1 compares two states before and after being exposed to a class, this information descriptor is qualified as a “thermodynamic feature” and relates to how much the signal’s transport is affected by the presence of a given environment compared to a reference, through a given material. Instead, α_2 uses a first-order derivative of time to quantify how fast or slow the signal decays or amplifies through a given material by the presence of a given environment: this information descriptor is qualified as a “kinetic feature”. Each feature is calculated for different scenarios of crossed-coupled environments/devices parameters, with a population of 24 different sensitive devices (composed of eight populations of sensitive materials measured on three different devices), exposed at 18 occurrences to different environments (six alternate permutations of three different solvent vapor exposures). The experimental details are fully described in a first study,[22] where the PCA was used exclusively with the feature α_1 calculated exclusively for the last ten seconds of each three-minute environment exposure. Although the steady-

state response for these materials was relatively fast compared to other materials for comparable tests,[24-27] the dataset totalizes over 44 hours of time acquisition assisted by manual operations to expose the different materials on different devices with different environments repeatedly to train the system. Applying the same approach for exposing $n!$ times the n different vapor classes for three minutes would yield to over a week, over a month and over seven months of total data acquisition, without interruption, to recognize respectively four, five and six different classes only. As reducing the number of materials, devices, or exposures would have consequences to degrade the recognition, it is straightforward to investigate on decreasing the elementary period for one single environment exposure to minimize the total acquisition duration. To assess on the classifier performances for a reduced acquisition time, a same dataset is considered, where data are pruned to ten seconds per acquisition sequences, after the exposure starts in order to make sure that the recognition performances do not depend on the acquisition itself, keeping the same number of datapoint to analyze in each case. Also, PCA/k-means was systematically used on all the different case scenario with the same normalization and initialization settings to not bias the clustering by user-dependent factors. The recognition after clustering uses the same rules and thresholds in each case, to assess a data sample as successfully, uncertainly or unsuccessfully recognized. All the individual PCA analysis are provided as supplementary information.

Steady-Resistance Modulation as a Thermodynamic Information Feature.

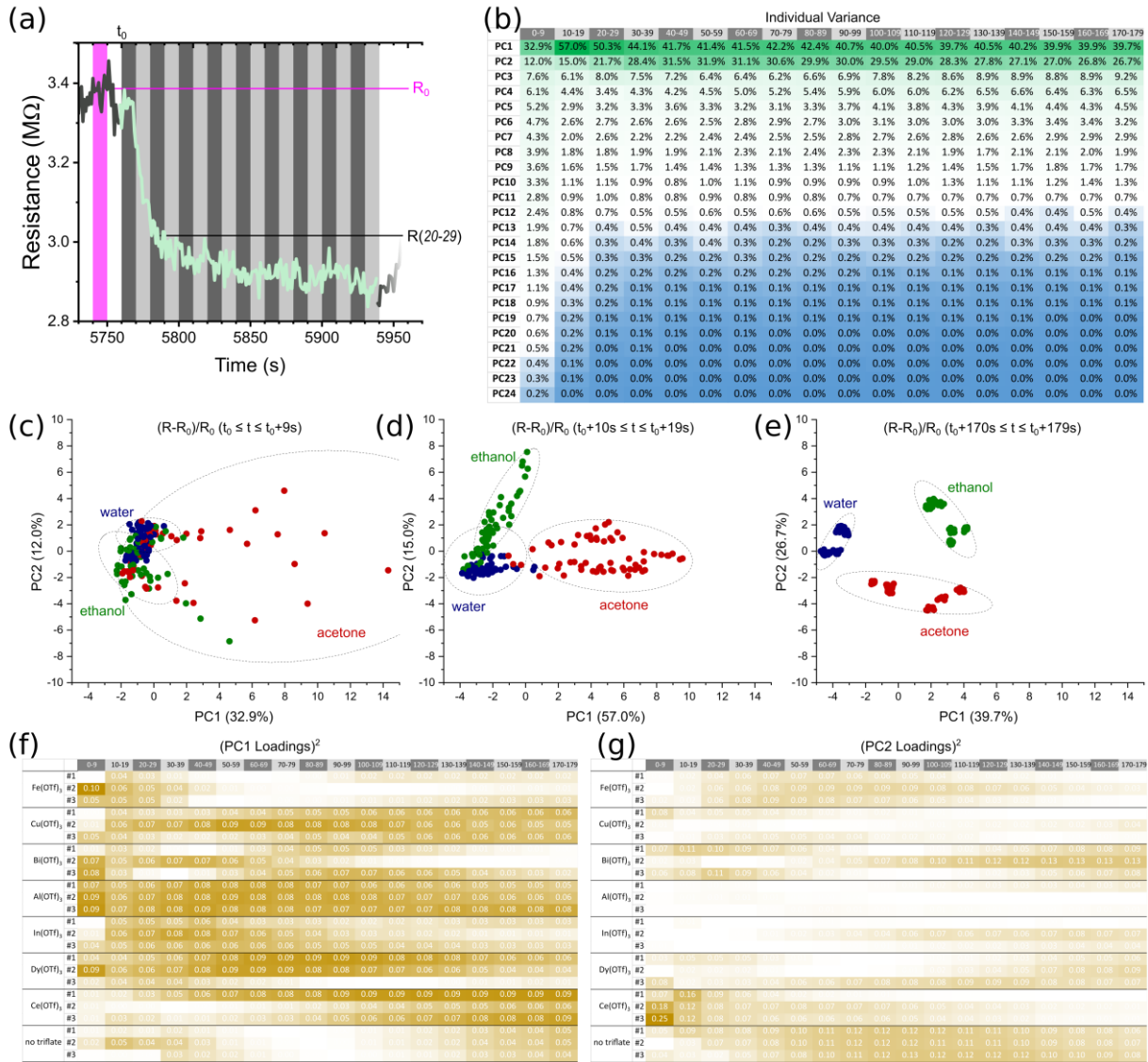


Figure 2. Analysis of the Relative Resistance Modulation as Information Descriptor | **a**, Extraction of the R_0 (as average for ten resistance values recorded between 11 and 20 seconds before vapor exposure, starting at t_0) and R (as average for ten resistance values recorded between t and $t + 10$ seconds every 10 seconds after t_0), to evaluate the feature $\alpha_1 = (R - R_0)/R_0$. **b**, PC variance for different PCA on α_1 , where R is measured at different time interval $[t; t + 10s]$ after t_0 (the tricolor gradient shades linearly between the minimum and maximum value of the whole table). **c-e**, PCA scores on α_1 , where R is measured at different time interval $[0s; 9s]$ (**c**), $[10s; 19s]$ (**d**) and $[170s; 179s]$ (**e**) after t_0 (confidence ellipsoids are set to 95% probability). **f-g**, Squared loadings of PC1 (**f**) and PC2 (**g**) for different PCA on α_1 , where R is measured at different time interval $[t; t + 10s]$ after t_0 (the bicolor gradient shades linearly between the minimum and maximum value of the whole tables).

The first analysis was performed using α_1 as information descriptor (see Fig.2), as in the former studies using the same dataset.[22, 28] The choice for this specific feature was oriented by the hypothesis that the presence of volatile molecules modulates the polymer electrical conductance by interacting with its dopant shift its thermodynamic charge-transfer equilibrium.[22] As a thermodynamic property, the acquisition was set to three minutes per exposure, to provide enough time for all devices to reach a quasi-steady state of conductance (steady output currents at a constant applied voltage). Here from the whole dataset, 18 different sub-datasets were generated by segmenting the data to concatenation of sequences of ten seconds after each exposure starts at t_0 (ten datapoints per exposures, 180 datapoints per sub-datasets – see Fig.2a). For each exposure, the feature α_1 takes into account two values: the resistance measured between the considered time interval and a reference resistance value R_0 measured while unexposed just before gas exposure. In each case, PCA was performed for the different sub-datasets, with the individual variance for each PC of each PCA for the different acquisition time compiled in Fig.2b. From these values, one can observe that most of the variance (>66%) is explained within the first two PC, except for data generated during the first ten seconds after t_0 . It is also noticed that the variance for all 24 PC does not change significantly for acquisitions occurring 30 seconds after exposure (Fig.2b, the color shade encodes the variance values in linear scale), suggesting that the feature α_1 is not enriched for the data separation in (PC1;PC2) if exposures last longer than 30 seconds. As shows their scores in the (PC1;PC2) projection (Fig.2c), the PCA on α_1 during the first ten seconds acquisition, noted $\text{PCA}^{\alpha_1}_{0-9}$, embeds most variability from acetone exposures on PC1 compared to two other clusters of data for water and ethanol, which are almost entirely contained in the acetone confidence ellipsoid. Already for $\text{PCA}^{\alpha_1}_{10-19}$ (Fig.2d), acetone is completely separable from the other two gases, and some minor overlap remains between water and ethanol confidence ellipsoids. The final sequence $\text{PCA}^{\alpha_1}_{170-179}$ in Fig.2e shows an ideal clustering in the (PC1;PC2) projection, that was used in the former study for gas recognition.[22] The loadings of PC1 and PC2 do not significantly depend on the acquisition sequences, except for the first ten seconds (Fig.2f and 2g): Excluding the first ten seconds, deviations overtime are however noticed: for instance the contribution of $\text{Ce}(\text{OTf})_3$ -doped

devices increase monotonically in the $PC1^{\alpha_1}$, such as the contribution of pristine P3HT in the $PC2^{\alpha_1}$. This suggests that materials that help better for the (PC1;PC2) data separation but expresses slower than others do not necessarily enhances the clustering. The former study concluded on the exclusive basis of the $PCA^{\alpha_1}_{170-179}$ analysis, two and three materials were preferred for recognizing ethanol from acetone from water using α_1 as information descriptor.[22] Fig.2f and 2g show that such conclusion is highly acquisition-dependent (even for the same dataset considered), and that experiments performed with shorter time exposures might have concluded otherwise for the material selection. As such dependency on the sample acquisition time greatly conditions the preferred material choice for classification, it appears legitimate to investigate on a dynamical feature such as α_2 as better information descriptor for gas recognition with the same raw current data.

Drift resistance α_2 in conductometric eNoses is less often used as information descriptor, although it is worth noticing that most conventional techniques in analytical chemistry use dynamical information features as information descriptors, such as chromatography (retention time of molecules on a substrate) or surface-plasmon resonance (absorption/desorption kinetic constants of molecules on a substrate). In a material, drifts can often be associated to a memory effect that alters reversibly or irreversibly a structural property,[29-33] rather than the transduction of an environmental information in a device. In case such drift is irreversible, such behavior appears as a material instability due to ageing and is often associated as a drawback for the lifetime. However since such reactivity on the material is environmentally induced *per se*, it is legitimate to wonder whether the information quality is preserved despite its effect on the information carrier itself. As an example, Kiselev et al. showed that such resistance drift (two-time median-resistance increase over four years) on conductometric nose is totally decorrelated from the ability of the classifier to recognize a class, as the strong correlation between all sensing elements' resistance drift does not bias linear discriminant analysis.[34] Supposed that part of the useful information to recognize gases lies in the diffusion kinetic of the volatile molecules through the doped polymers, or the adsorption/desorption kinetic constants of the molecular gases on the doped materials under flow, the drift-resistance may be a relevant information descriptor as it takes into account the first derivative of time (Fig.3a). Replicating the same methodology as previously for relative resistance modulation, PCA on α_2 as information descriptor has been performed for the 18 different sub-datasets. As for α_1 , the evolution of the variance for the individual PC depends on the acquisition time (Fig.3b), mainly at the beginning of the transient response (typically the first 20 seconds). A singular difference with α_1 is the impoverishing in data variance on the first two PC with the increase of the acquisition time (from >66% for PCA $^{\alpha_1}_{170-179}$ down to <28% for PCA $^{\alpha_2}_{170-179}$). This was expected as the information becomes more sensitive to the signal's noise at the reach of the steady-state, and therefore, with the increase of the acquisition time decreases the contribution of the molecularly-specific response compared in the overall information. We noticed also in Fig.3b that significantly less variance is contained in PC2 $^{\alpha_2}$ compared to PC2 $^{\alpha_1}$, and

more importantly that variance for $PC2^{\alpha 2}$ is far less dependent on the acquisition time than $PC2^{\alpha 1}$. This suggests that despite any quality for the recognition, α_2 seems to separate data mostly because of one single parameter (if a linear model is considered), while α_1 seems to depend from mostly two parameters of a linear model. On the quality of the data separation (Fig.3c-e), similar trends for the (PC1;PC2) diagrams are observed depending on the acquisition time: At the first ten seconds of time acquisition after t_0 , acetone data are better separated from the rest, followed by the ethanol data. Confidence ellipsoids seem to be always overlapping one another, however, we observed that even until three minutes after time t_0 that the three volatile compounds are still recognizable, despite the residual dynamic of the sensing elements. It is also noticed that $PCA^{\alpha 2}_{170-179}$ (Fig.3e) clusters are more homogeneous than the ones of $PCA^{\alpha 1}_{170-179}$ (Fig.2e): smaller clusters within each ellipsoids can be distinguished in $PCA^{\alpha 1}_{170-179}$, which are attributed to experimental biases of the six repeated exposures for each classes. The dependency of $PCA^{\alpha 2}$ loadings with the acquisition time displays different trends than the one for $PCA^{\alpha 1}$ loadings (Fig.3g-h). For the first 20 s, all sensing elements except the ones coated with pristine P3HT and $Ce(OTf)_3$ -doped P3HT seem to have a comparable contribution in the $PC1^{\alpha 2}$ and the $Ce(OTf)_3$ -doped P3HT coated devices mostly constitute $PC2^{\alpha 2}$ if $t-t_0 < 20$ s. From 20 s after t_0 , $Ce(OTf)_3$ -doped P3HT coated devices become the most significant in the $PC1^{\alpha 2}$, while $PC2^{\alpha 2}$ loadings seem highly random if $t-t_0 < 20$ s. This closer look on the $PC1^{\alpha 2}$ and $PC2^{\alpha 2}$ loading highlights two different dynamics that successfully help in identifying the volatile compounds: before 20 seconds, a “fast” and a “slow” dynamics yields the array response to recognize all three classes from $PC1^{\alpha 2}$ and $PC2^{\alpha 2}$. After 20 seconds, the fast dynamic of all sensing elements have faded away, to leave a minor contribution on the $Ce(OTf)_3$ -doped P3HT devices exclusively.

Steady vs Dynamical Resistance for Gas Recognition.

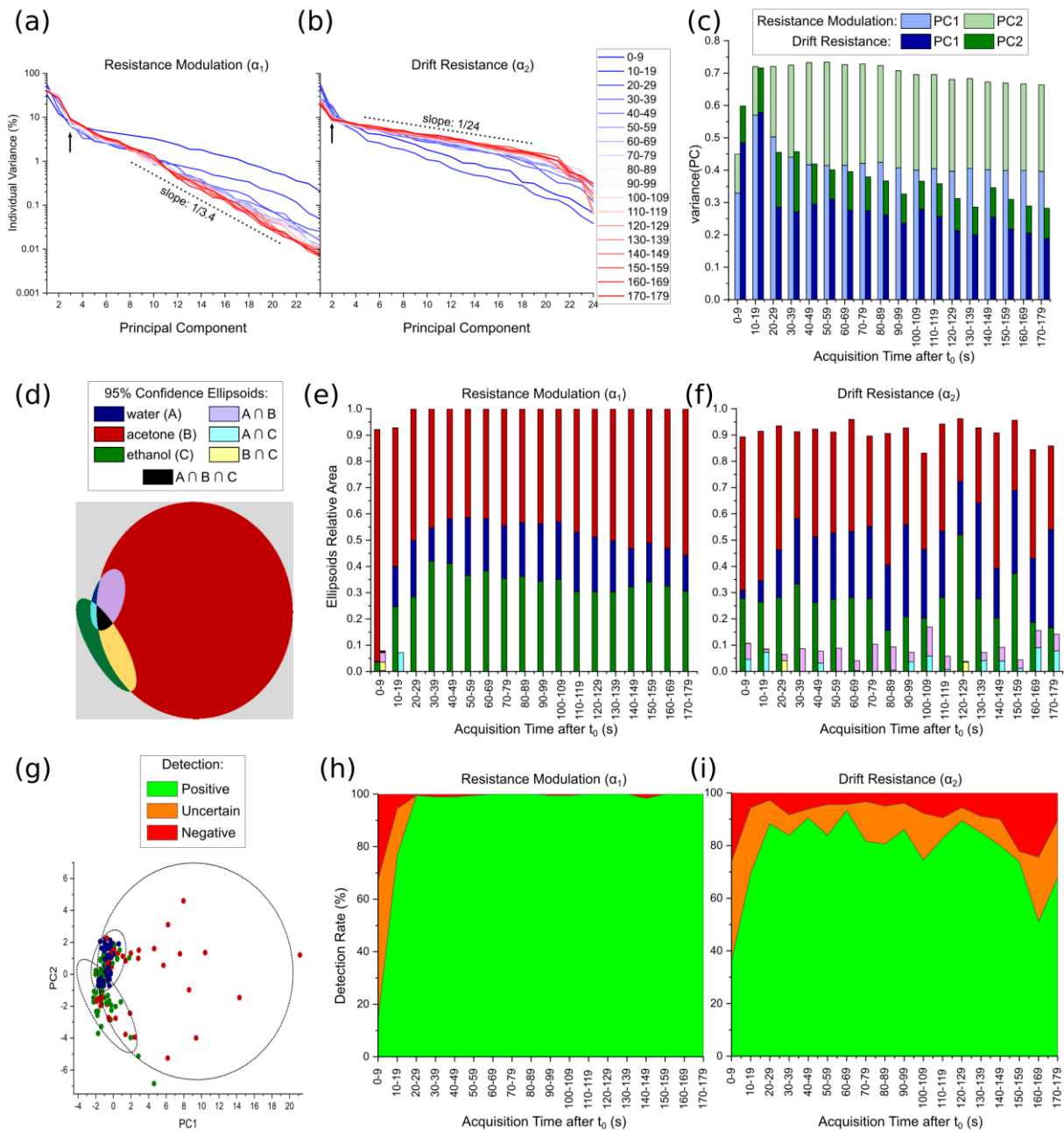


Figure 4. Comparison of Both Descriptors | **a-b**, Scree plots for the PCA performed with different acquisition times, from the first ten seconds after t_0 (“0-9” in blue) to the last ten seconds after t_0 (“170-179” in red), performed with either the relative resistance modulation - α_1 (a) or the drift resistance - α_2 (b) as information descriptor. **c**, Explained variance for PC1 and PC2 with PCA performed for different acquisition time with either α_1 or α_2 . **d-f**, Overlap area of the three 95%-confidence ellipsoids in (PC1,PC2), for PCA performed for different acquisition time with either α_1 or α_2 . The area were estimated by discretizing the different regions where the three ellipsoids are segmented in the smallest square of 500x500 pixels. In figure d is displayed the example for the PCA with α_2 for the “0-9” time acquisition and the histograms of the ellipsoids relative area as a function of the acquisition time for α_1 and for α_2 are respectively displayed in figure e and figure f. **g-i**, Detection tests of the PCA scores, for PCA performed for different acquisition time with either α_1 or α_2 . The test is considered positive, uncertain and negative, respectively when scores are exclusively inside, not-exclusively inside and outside the corresponding 95%-confidence ellipsoid. In figure g is displayed the example for the PCA

with α_2 for the “0-9” time acquisition and the graphs of the detection rate as a function of the acquisition time for α_1 and for α_2 are respectively displayed in figure h and figure i.

To qualitatively compare the total variance distributions over the different PC with either α_1 or α_2 as information descriptor, the Scree plots are displayed on two different graphs and shows the effect of the acquisition time after t_0 for both descriptors (Fig.4a and Fig.4b). Both of them confirm the trend of the variance with the acquisition time, for all principal components (not PC1 and PC2 exclusively). As Fig.4a shows, the increase of the acquisition time after exposure at t_0 tends to diminish the variance contained at the lowest PC in case of considering α_1 as information descriptor, while it tends to increase the variance of the lower PC in case of considering α_2 as information descriptor in Fig.4b. We observed that this diminishing rate is different for both descriptors as displayed in Fig.4a and Fig.4b, which might come from bias between the linear *ad hoc* model computed by the PCA and the actual physical model that governs the dependency of the information descriptors on the different sensing elements. The position of the elbows on both plots (indicated by arrows on the Scree plots in Fig.4a and Fig.4b) confirms that most of the useful variance for PCA^{α_1} is contained within the first three PC, while only the first two for PCA^{α_2} . Particularly for the drift resistance α_2 , this elbow is highly acquisition dependent, and one may appreciate a richer model with more PC to account for shorter acquisition time. The variance analysis on PC1 and PC2 for both PCA^{α_1} and PCA^{α_2} shows an acquisition time optimal to contain most of the data variance in both PC1 and PC2 independently from the chosen information descriptor (Fig.4c). The histogram displayed in Fig.4c shows that if the acquisition time is set at the transient between 10 and 19 s after t_0 , both information features can gather at least 70% of the total variance in two different biparametric linear models. As both information features show opposed trends in the PC1+PC2 variance evolution with the acquisition time, it was expected to observe an acquisition-time optimum for both PCA, independently from the quality of the data clustering. To quantify the recognition performances of the sensing array with PCA^{α_1} and PCA^{α_2} , the confidence ellipsoids determined by k-means clustering are used as a threshold to declare whether the given data belong to a given class or not, to define seven classes (as displayed in Fig.4d). The relative area of the overlap for the confidence ellipsoids has been evaluated for the different acquisition time and

displayed in two different histograms for each descriptor in Fig.4d-f. For α_1 (Fig.4e), one can observe that ellipsoids do not overlap from $t-t_0 > 20$ s, while in the case of α_2 (Fig.4f), confidence ellipsoids always overlap one another at any time for the acquisition. However, it should be noticed that the overlap in each case is only moderate: with less than 20% of the total area of the ellipsoids. This suggests that recognition tests may be higher in case α_1 is used as information descriptor, than for α_2 . To verify this, recognition tests have been performed on the same sub-datasets, using the 95%-confidence ellipsoids as threshold for classification (Fig.4g-i). Detection is considered as “positive” if the actual class of the PCA score is exclusively contained within the corresponding confidence ellipsoid, “uncertain” if the actual class of the PCA score is not exclusively contained within the corresponding confidence ellipsoid, and “negative” if the actual class of the PCA score is excluded from the corresponding confidence ellipsoid. On the one hand for α_1 (Fig.4h), one can observe that the positive detection rate $99.4 \pm 0.6\%$ for acquisition time higher than 20 s after t_0 . On the one hand for α_2 (Fig.4i), one can observe that the positive detection rate $>80\%$ for acquisition times higher between 20 s and 149 s after t_0 . However, we noticed that using α_2 as information descriptor enables substantially better recognition than α_1 for short acquisition time below 10 s after t_0 : typically, 36% positive and 38% uncertain using α_2 , while 14% positive and 53% uncertain using α_1 . Overall, this statistical study support that the different materials used in the array allow recognizing volatile organic compounds because of the relative resistance modulation (α_1), rather than the resistance drift (α_2), and points out the thermodynamic of the current modulations rather than the kinetic involved in the process.

Discussion

Although this study focuses specifically on doped conducting polymers, the approach is generic to any conductometric eNose and could have been addressed to different class of conducting materials used as transducers in an array. Despite the fact that α_1 and α_2 are frequently used as information descriptors for such application, our study proposes to investigate on which feature gather most of the useful information for an eNose. However, we want to highlight that for practical applications, such a choice may be conditioned rather by the application than the quality of the data *per se*. Specifically for the resistance modulation α_1 , the feature needs to routinely set a reference resistance R_0 , when the environment is considered “neutral” between each data sampling. This requires therefore to have a hand on the sample exposure to periodically regenerate the device from a stimuli: it is therefore practically more convenient to use α_1 as information descriptor in cases where analytes can be exposed to a system in a supervised manner (to evaluate fragrance batch quality in an analytical laboratory for instances). Such thermodynamic feature seems practically inadequate to extract for environment recognition in case the system is permanently exposed without periodic regeneration. For the drift resistance α_2 , the feature does not depend on a buffered reference. However, a steady value of the sampling period must be set to measure the dynamic: it is therefore a more adequate feature for online inference for environment recognition, at the condition that the sampling period is set *a posteriori* given the dynamic of the pattern to recognize. It is therefore a more adequate feature to recognize stimuli that are governed by a rhythm (for instance, pollution cycles in urban environments for instance). Here in this study, the selection of these features α_1 and α_2 is not based on the practical convenience to compute them in a conductometric eNose application, but on the quality of the data they output for conducting polymers used in a recognition tests that conveniently enables computing both of them at will.

In such framework, PCA confirmed that the useful information in the current response of conducting polymer materials, doped with different metal triflates and exposed to different volatile

organic compounds, lies specifically in the thermodynamic of the device resistance modulation and not its kinetic. The analysis of the relative resistance modulation α_1 is more robust overtime when analyzed 20 seconds after each exposures at t_0 : the first two PC explains at least two third of the data variance and allows an optimal clustering without overlap and enables $99.4 \pm 0.6\%$ recognition. Considering that all devices have the same geometry, mechanisms responsible for the modulation of the electrical resistivity are pointed out. As different doping effects were assessed by varying the nature of the dopant,[22] modulation of the doping yield, by the interaction of different volatile molecules as electron-donating ligands on an electrophilic Lewis acid,[35-37] is not invalidated by this analysis. The statistical approach does not allow discriminating between the effect on the charge carrier density or the charge carrier mobility for the different materials exposed to different gases. Despite the fact that materials' conductivity is function of two independent physical properties (the charge carrier density and the charge carrier mobility), one cannot conclude that any of these properties are purely marking $PC1^{\alpha_1}$ and $PC2^{\alpha_1}$, since conductivity is the product of both and PCA scores are linear combinations of PC. Such investigation could be carried out using the logarithmic value of the resistance modulation $\alpha_3 = \log(R/R_0)$ as information descriptor for the PCA, in order to assess the individual contributions of the carrier mobility " μ " and carrier density " n " as principal components, since $\alpha_3 = \log(n_0/n) + \log(\mu_0/\mu)$. Such validation would have to be confirmed by correlating the PC^{α_3} loadings with systematic study of carrier density and mobility assessment, in another study that couples this approach with further material characterizations.

Conclusion

By statistical analysis, we evidenced that the relative resistance modulation of a doped conducting polymer array is a better information descriptor than the drift resistance, to recognize volatile organic compounds with different metal-triflate doped polythiophene sensing elements. This shows that the information carrier for the molecular recognition using these materials in an electronic nose is rather linked to the thermodynamic equilibrium that yields the doped conducting polymers' conductivity with its environment, rather than kinetic limitations which would select molecular targets' based on their drift diffusion through different doped polymers. Despite this result suggesting to wait for a complete steady state for each sensing element response, we evidenced that the thermodynamic properties to recognize molecular gases lies already in the transience of the material response. Despite materials reach a fast quasi-steady response within three minutes of environment exposures, principal component analysis and k-means clustering show that the recognition is already higher than 99% after only 20 seconds of gas exposures. This suggests that training time to recognize molecular environment can greatly be optimized for practical applications, even in the case conducting materials in an electronics nose show slow response. Applied for practical recognition with an eNose, this approach to find a preliminary optimum for data acquisition before test shall greatly increase information throughputs for using eNose for chemical quality assessments by reducing the training duration while preserving most of the data quality to train an eNose to recognize various volatile molecular patterns.

Supporting Information

Supplementary information is available in the online version of the paper.

Acknowledgements

SP thanks the French Research Agency (ANR) for funding the “Sensation” project (Grant # ANR-22-CE24-0001-01). The authors thank the French Nanofabrication Network RENATECH for financial support of the IEMN cleanroom.

Competing Interests

The authors declare no competing interests.

References

1. Persaud, K.C., A.M. Pisanelli, and P. Evans, *Medical diagnostics and health monitoring*. Handbook of Machine Olfaction: Electronic Nose Technology, 2002: p. 445-460. ([DOI:10.1002/3527601597.ch18](https://doi.org/10.1002/3527601597.ch18))
2. Karakaya, D., O. Ulucan, and M. Turkan, *Electronic nose and its applications: A survey*. International journal of Automation and Computing, 2020. **17**(2): p. 179-209. . ([DOI: 10.1007/s11633-019-1212-9](https://doi.org/10.1007/s11633-019-1212-9))
3. Cheng, L., et al., *Development of compact electronic noses: A review*. Measurement Science and Technology, 2021. **32**(6): p. 062002. ([DOI 10.1088/1361-6501/abef3b](https://doi.org/10.1088/1361-6501/abef3b))
4. Illahi, A.A.C., et al. *Electronic Nose Technology and Application: A Review*. in *2021 IEEE 13th International Conference on Humanoid, Nanotechnology, Information Technology, Communication and Control, Environment, and Management (HNICEM)*. 2021. IEEE. ([DOI: 10.1109/HNICEM54116.2021.9731890](https://doi.org/10.1109/HNICEM54116.2021.9731890))
5. Liu, T., et al., *Review on Algorithm Design in Electronic Noses: Challenges, Status, and Trends*. Intelligent Computing, 2023. **2**: p. 0012. ([DOI: epdf/10.34133/icomputing.0012](https://doi.org/epdf/10.34133/icomputing.0012))
6. Ruddigkeit, L., et al., *Enumeration of 166 billion organic small molecules in the chemical universe database GDB-17*. Journal of chemical information and modeling, 2012. **52**(11): p. 2864-2875. ([DOI:10.1021/ci300415d](https://doi.org/10.1021/ci300415d))
7. Bühlmann, S. and J.-L. Reymond, *ChEMBL-likeness score and database GDBChEMBL*. Frontiers in chemistry, 2020. **8**: p. 46. ([DOI:10.3389/fchem.2020.00046](https://doi.org/10.3389/fchem.2020.00046))
8. Hierlemann, A. and R. Gutierrez-Osuna, *Higher-order chemical sensing*. Chemical reviews, 2008. **108**(2): p. 563-613. ([DOI:10.1021/cr068116m](https://doi.org/10.1021/cr068116m))
9. Peveler, W.J., M. Yazdani, and V.M. Rotello, *Selectivity and specificity: pros and cons in sensing*. ACS sensors, 2016. **1**(11): p. 1282-1285. ([DOI:10.1021/acssensors.6b00564](https://doi.org/10.1021/acssensors.6b00564))
10. Parastar, H. and D. Kirsanov, *Analytical figures of merit for multisensor arrays*. ACS sensors, 2020. **5**(2): p. 580-587. ([DOI: abs/10.1021/acssensors.9b02531](https://doi.org/abs/10.1021/acssensors.9b02531))
11. Alsaedi, B.S., et al., *Multivariate limit of detection for non-linear sensor arrays*. Chemometrics and Intelligent Laboratory Systems, 2020. **201**: p. 104016. ([DOI: abs/10.1021/acssensors.9b02531](https://doi.org/abs/10.1021/acssensors.9b02531))
12. Hatfield, J., et al., *Towards an integrated electronic nose using conducting polymer sensors*. Sensors and Actuators B: Chemical, 1994. **18**(1-3): p. 221-228. ([DOI: 10.1016/j.chemolab.2020.104016](https://doi.org/10.1016/j.chemolab.2020.104016))
13. Chiu, S.-W. and K.-T. Tang, *Towards a chemiresistive sensor-integrated electronic nose: a review*. Sensors, 2013. **13**(10): p. 14214-14247. ([DOI :10.3390/s131014214](https://doi.org/10.3390/s131014214))
14. Park, S.Y., et al., *Chemoresistive materials for electronic nose: Progress, perspectives, and challenges*. InfoMat, 2019. **1**(3): p. 289-316. . ([DOI :10.1002/inf2.12029](https://doi.org/10.1002/inf2.12029))
15. Sierra-Padilla, A., et al., *E-Tongues/noses based on conducting polymers and composite materials: Expanding the possibilities in complex analytical sensing*. Sensors, 2021. **21**(15): p. 4976. ([DOI: .org/10.3390/s21154976](https://doi.org/10.3390/s21154976))
16. Bedoui, S., et al. *Electronic nose system and principal component analysis technique for gases identification*. in *10th International Multi-Conferences on Systems, Signals & Devices 2013 (SSD13)*. 2013. IEEE. . ([DOI: 10.1109/SSD.2013.6564152](https://doi.org/10.1109/SSD.2013.6564152))
17. Yin, Y. and Y. Zhao, *A feature selection strategy of E-nose data based on PCA coupled with Wilks A-statistic for discrimination of vinegar samples*. Journal of Food Measurement and Characterization, 2019. **13**: p. 2406-2416. ([DOI: 10.1007/s11694-019-00161-0](https://doi.org/10.1007/s11694-019-00161-0))
18. Bakar, M., et al. *Electronic Nose Testing for Confined Space Application Utilizes Principal Component Analysis and Support Vector Machine*. in *IOP Conference Series: Materials Science and Engineering*. 2020. IOP Publishing. ([DOI: 10.1088/1757-899X/932/1/012072](https://doi.org/10.1088/1757-899X/932/1/012072))

19. Nagle, H.T. and S.S. Schiffman, *Electronic taste and smell: The case for performance standards [point of view]*. Proceedings of the IEEE, 2018. **106**(9): p. 1471-1478. ([DOI:10.1109/IEEESTD.2018.8277147](https://doi.org/10.1109/IEEESTD.2018.8277147))
20. Pecqueur, S., et al., *Neuromorphic time-dependent pattern classification with organic electrochemical transistor arrays*. Advanced Electronic Materials, 2018. **4**(9): p. 1800166. ([DOI:10.1002/aelm.201800166](https://doi.org/10.1002/aelm.201800166))
21. Pecqueur, S., et al., *A Neural Network to Decipher Organic Electrochemical Transistors' Multivariate Responses for Cation Recognition*. Electronic Materials, 2023. **4**(2): p. 80-94. ([DOI:10.3390/electronicmat4020007](https://doi.org/10.3390/electronicmat4020007))
22. Boujnah, A., et al., *Mildly-doped polythiophene with triflates for molecular recognition*. Synthetic Metals, 2021. **280**: p. 116890. ([DOI:10.1016/j.synthmet.2021.116890](https://doi.org/10.1016/j.synthmet.2021.116890))
23. Metsalu, T. and J. Vilo, *ClustVis: a web tool for visualizing clustering of multivariate data using Principal Component Analysis and heatmap*. Nucleic acids research, 2015. **43**(W1): p. W566-W570. ([DOI:10.1093/nar/gkv468](https://doi.org/10.1093/nar/gkv468))
24. Peng, G., E. Trock, and H. Haick, *Detecting simulated patterns of lung cancer biomarkers by random network of single-walled carbon nanotubes coated with nonpolymeric organic materials*. Nano letters, 2008. **8**(11): p. 3631-3635. ([DOI:10.1021/nl801577u](https://doi.org/10.1021/nl801577u))
25. Kumar, S., et al., *Thin film chemiresistive gas sensor on single-walled carbon nanotubes-functionalized with polyethylenimine (PEI) for NO₂ gas sensing*. Bulletin of Materials Science, 2020. **43**: p. 1-7. ([DOI:10.1007/s12034-020-2043-6](https://doi.org/10.1007/s12034-020-2043-6))
26. Kanaparthy, S. and S.G. Singh, *Reduction of the measurement time of a chemiresistive gas sensor using transient analysis and the cantor pairing function*. ACS Measurement Science Au, 2021. **2**(2): p. 113-119. ([DOI:10.1021/acsmeasuresciau.1c00043](https://doi.org/10.1021/acsmeasuresciau.1c00043))
27. Freddi, S., et al., *A Chemiresistor sensor array based on graphene nanostructures: From the detection of ammonia and possible interfering VOCs to chemometric analysis*. Sensors, 2023. **23**(2): p. 882. ([DOI:10.3390/s23020882](https://doi.org/10.3390/s23020882))
28. Boujnah, A., et al., *An electronic nose using conductometric gas sensors based on P3HT doped with triflates for gas detection using computational techniques (PCA, LDA, and kNN)*. Journal of Materials Science: Materials in Electronics, 2022. **33**(36): p. 27132-27146. ([DOI:10.1007/s10854-022-09376-2](https://doi.org/10.1007/s10854-022-09376-2))
29. Li, J., B. Luan, and C. Lam. *Resistance drift in phase change memory*. in *2012 IEEE International Reliability Physics Symposium (IRPS)*. 2012. IEEE. ([DOI:10.1109/IRPS.2012.6241871](https://doi.org/10.1109/IRPS.2012.6241871))
30. Paredes-Madrid, L., et al., *Underlying physics of conductive polymer composites and force sensing resistors (FSRs). A study on creep response and dynamic loading*. Materials, 2017. **10**(11): p. 1334. ([DOI:10.3390/ma10111334](https://doi.org/10.3390/ma10111334))
31. Chen, Y., et al., *Chemical understanding of resistance drift suppression in Ge–Sn–Te phase-change memory materials*. Journal of Materials Chemistry C, 2020. **8**(1): p. 71-77. ([DOI:10.1039/C9TC04810C](https://doi.org/10.1039/C9TC04810C))
32. Pries, J., et al., *Resistance Drift Convergence and Inversion in Amorphous Phase Change Materials*. Advanced Functional Materials, 2022. **32**(48): p. 2207194. ([DOI:10.1002/adfm.202207194](https://doi.org/10.1002/adfm.202207194))
33. Müller, G. and G. Sberveglieri, *Origin of Baseline Drift in Metal Oxide Gas Sensors: Effects of Bulk Equilibration*. Chemosensors, 2022. **10**(5): p. 171. ([DOI:10.3390/chemosensors10050171](https://doi.org/10.3390/chemosensors10050171))
34. Kiselev, I., et al. *On the Temporal Stability of Analyte Recognition with an E-Nose Based on a Metal Oxide Sensor Array in Practical Applications*. Sensors 2018, **18**, 550. ([DOI:10.3390/s18020550](https://doi.org/10.3390/s18020550))
35. Pecqueur, S., *Lewis Acid-Base Theory Applied on Evaluation of New Dopants for Organic Light-Emitting Diodes*. 2014: Friedrich-Alexander-Universitaet Erlangen-Nuernberg (Germany).

36. Pecqueur, S., et al., *Wide Band-Gap Bismuth-based p-Dopants for Opto-Electronic Applications*. *Angewandte Chemie International Edition*, 2016. **55**(35): p. 10493-10497. ([DOI:10.1002/anie.201601926](https://doi.org/10.1002/anie.201601926))
37. Ferchichi, K., et al., *Concentration-control in all-solution processed semiconducting polymer doping and high conductivity performances*. *Synthetic Metals*, 2020. **262**: p. 116352. ([DOI: 10.1016/j.synthmet.2020.116352](https://doi.org/10.1016/j.synthmet.2020.116352))

Supporting Information for:

Steady vs. Dynamic Contributions of Different Doped Conducting Polymers in the Principal Components of an Electronic Nose's Response

Wiem Haj Ammar^a, Aicha Boujnah^a, Aimen Boubaker^a, Adel Kalboussi^a, Kamal Lmimouni^b & Sébastien Pecqueur^{b*},

^a Department of Physics, University of Monastir Tunisia.

^b Univ. Lille, CNRS, Centrale Lille, Univ. Polytechnique Hauts-de-France, UMR 8520 - IEMN, F-59000 Lille, France.

Email: sebastien.pecqueur@iemn.fr

PCA scores (a), variance for the different PC (b) and their loadings (c) are organized in the different supporting figures by acquisition time for both information descriptors α_1 and α_2 such as:

		Descriptors	
		α_1	α_2
Acquisition Time Interval (in seconds)	[0;9]	Figure S1	Figure S19
	[10;19]	Figure S2	Figure S20
	[20;29]	Figure S3	Figure S21
	[30;39]	Figure S4	Figure S22
	[40;49]	Figure S5	Figure S23
	[50;59]	Figure S6	Figure S24
	[60;69]	Figure S7	Figure S25
	[70;79]	Figure S8	Figure S26
	[80;89]	Figure S9	Figure S27
	[90;99]	Figure S10	Figure S28
	[100;109]	Figure S11	Figure S29
	[110;119]	Figure S12	Figure S30
	[120;129]	Figure S13	Figure S31
	[130;139]	Figure S14	Figure S32
	[140;149]	Figure S15	Figure S33
	[150;159]	Figure S16	Figure S34
	[160;169]	Figure S17	Figure S35
	[170;179]	Figure S18	Figure S36

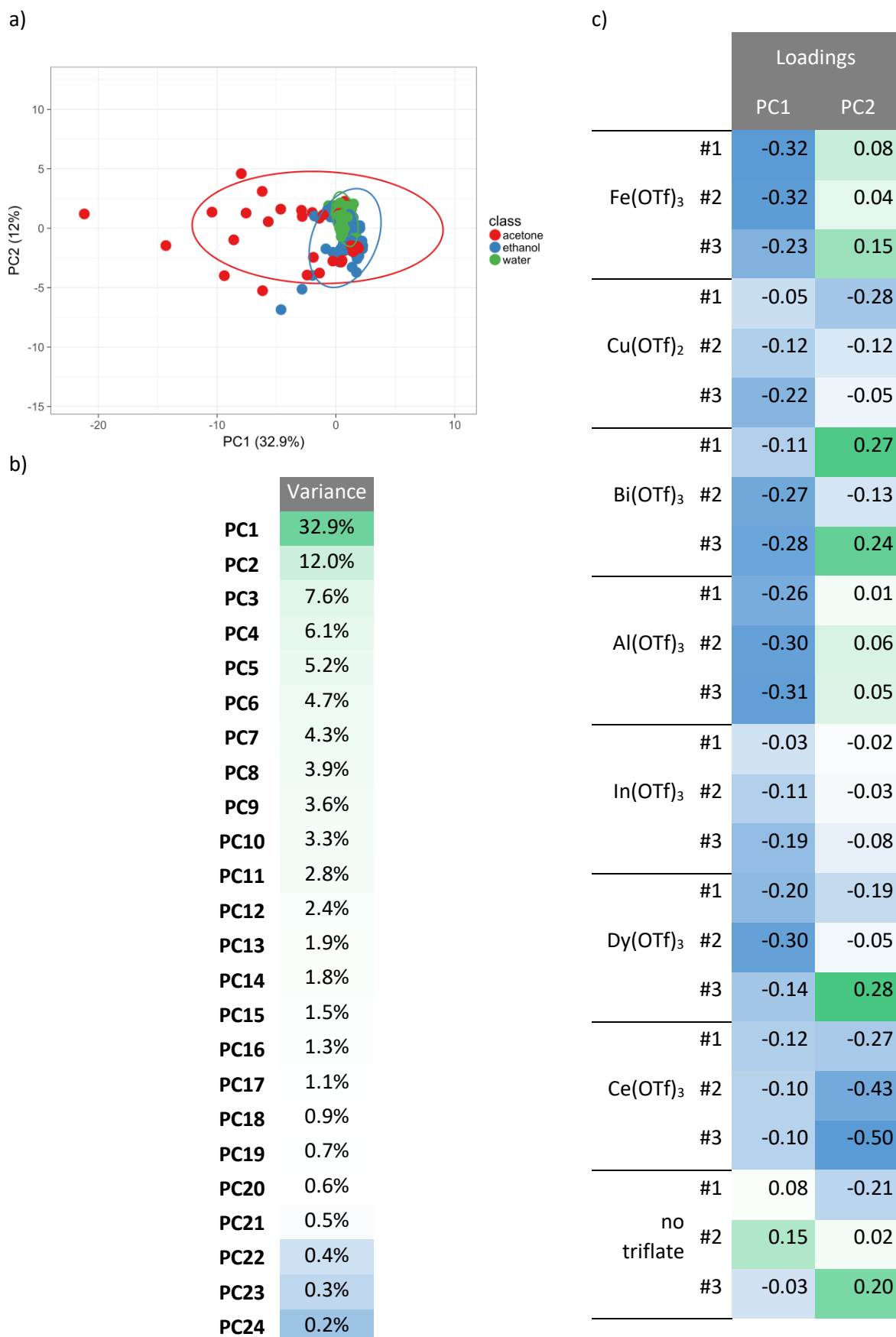


Figure S1. PCA on α_1 , for R is measured at different time interval [0s;9s] | a, PCA scores with 95% confidence ellipsoids. b, Individual variance for the different PC. c, PCA loadings of the different sensing elements' response for PC1 and PC2.

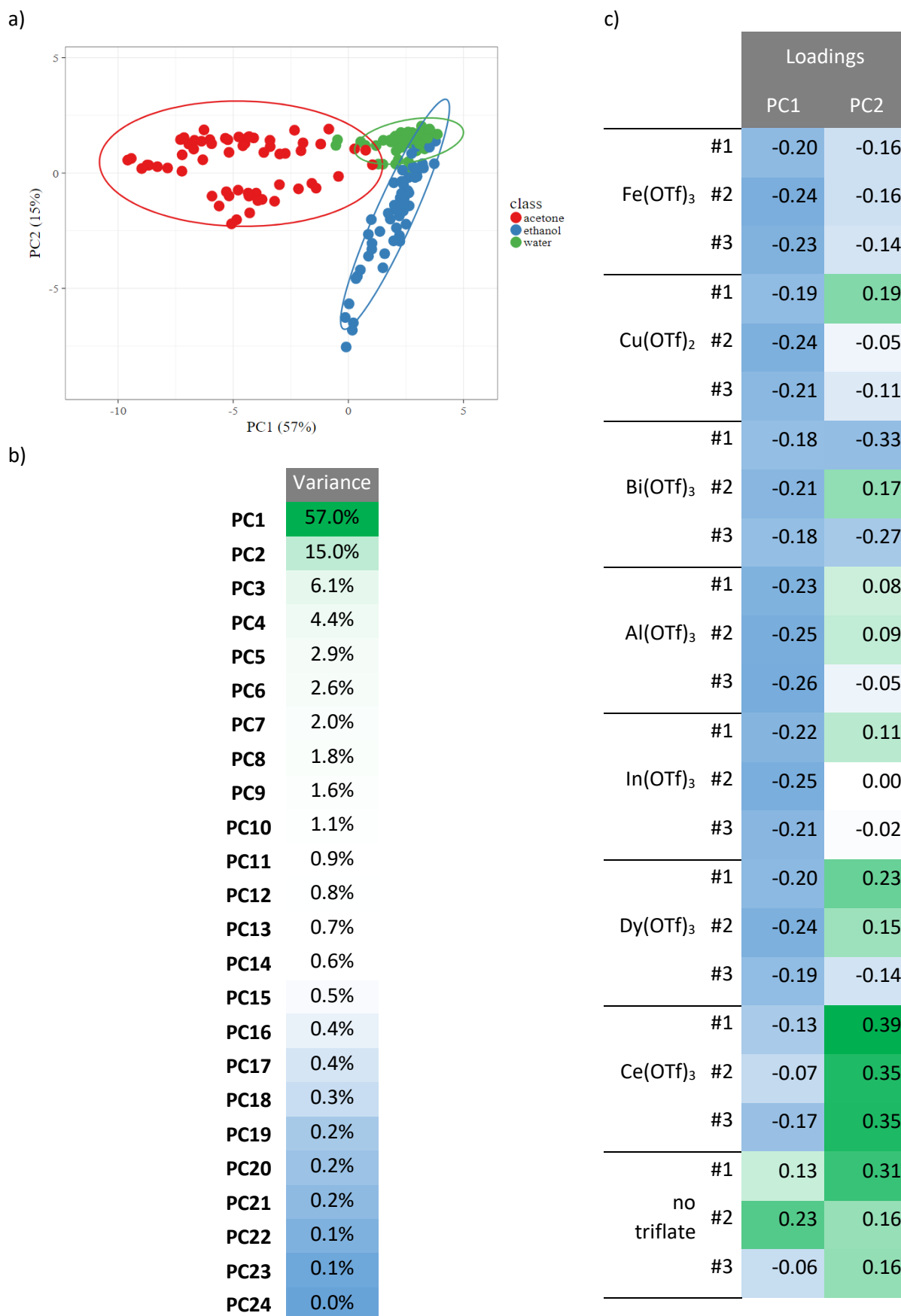


Figure S2. PCA on α_1 , for R is measured at different time interval [10s;19s] | a, PCA scores with 95% confidence ellipsoids. b, Individual variance for the different PC. c, PCA loadings of the different sensing elements' response for PC1 and PC2.

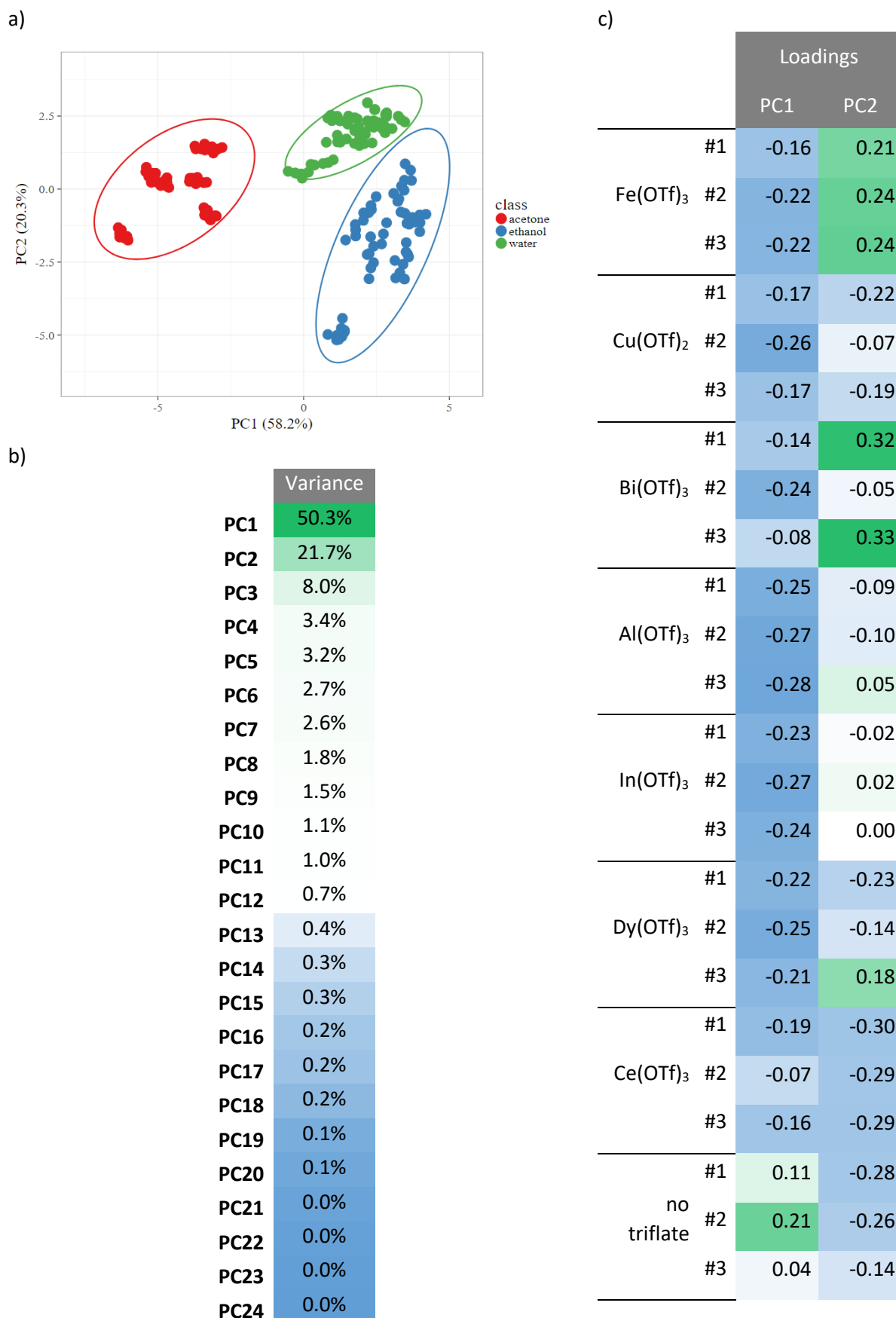


Figure S3. PCA on α_1 , for R is measured at different time interval [20s;29s] | **a**, PCA scores with 95% confidence ellipsoids. **b**, Individual variance for the different PC. **c**, PCA loadings of the different sensing elements' response for PC1 and PC2.

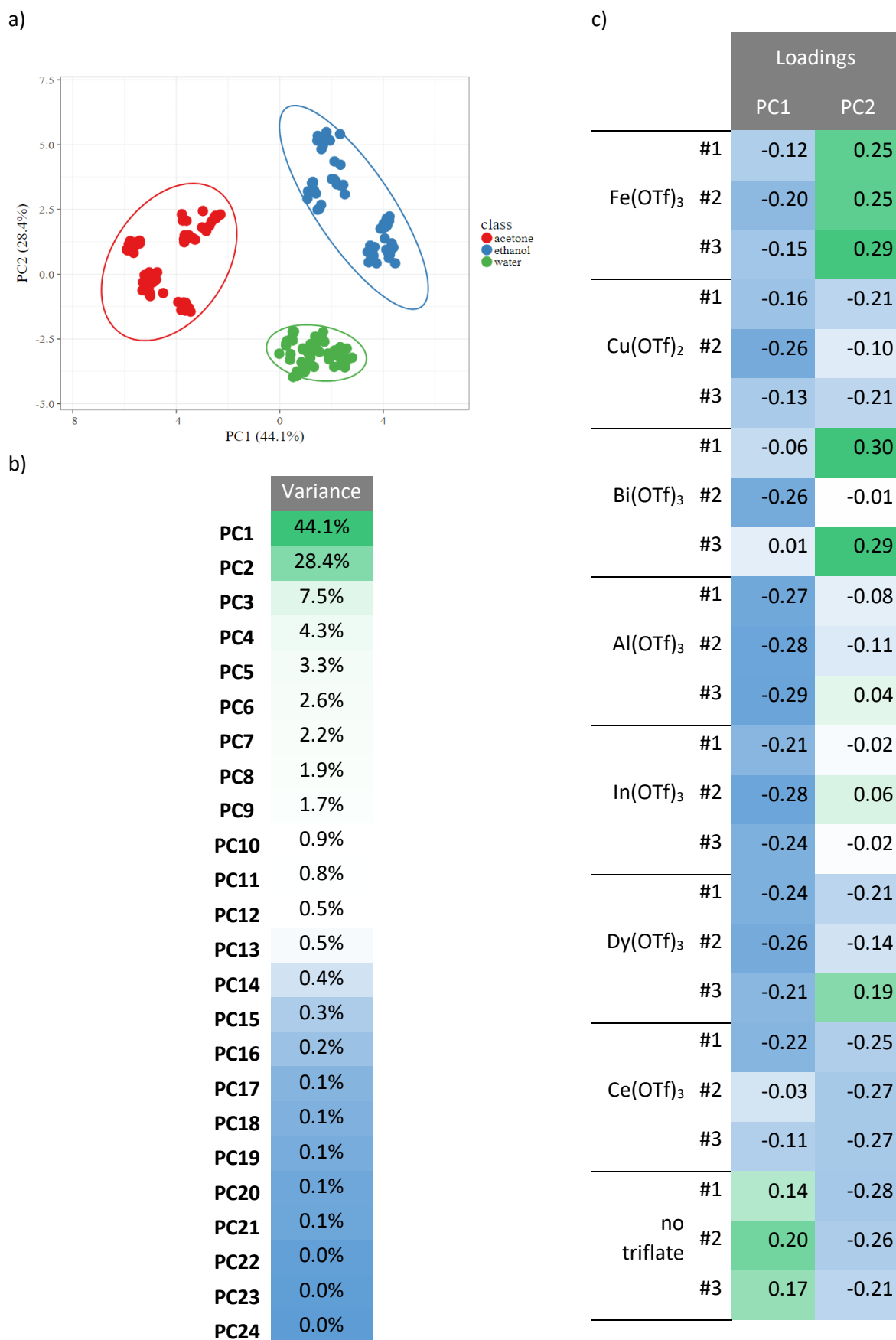
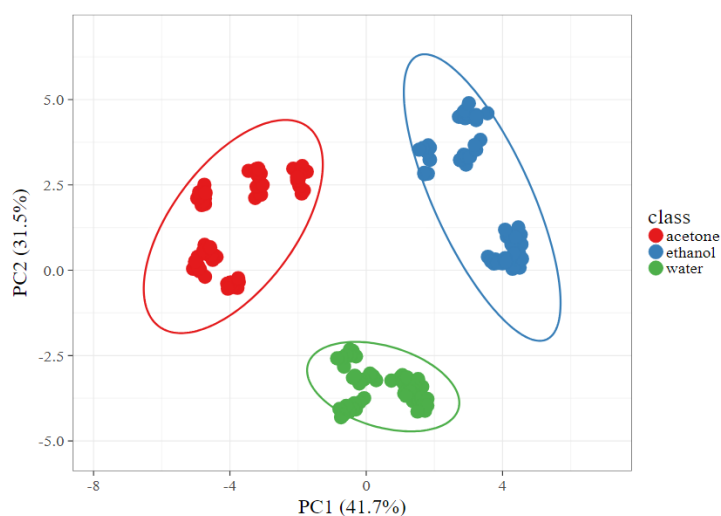


Figure S4. PCA on α_1 , for R is measured at different time interval [30s;39s] | **a**, PCA scores with 95% confidence ellipsoids. **b**, Individual variance for the different PC. **c**, PCA loadings of the different sensing elements' response for PC1 and PC2.

a)



b)

	Variance
PC1	41.7%
PC2	31.5%
PC3	7.2%
PC4	4.2%
PC5	3.6%
PC6	2.6%
PC7	2.2%
PC8	1.9%
PC9	1.4%
PC10	0.8%
PC11	0.8%
PC12	0.5%
PC13	0.4%
PC14	0.3%
PC15	0.2%
PC16	0.2%
PC17	0.1%
PC18	0.1%
PC19	0.1%
PC20	0.1%
PC21	0.0%
PC22	0.0%
PC23	0.0%
PC24	0.0%

c)

		Loadings	
		PC1	PC2
Fe(OTf) ₃	#1	-0.07	0.26
	#2	-0.15	0.28
	#3	-0.05	0.31
Cu(OTf) ₂	#1	-0.17	-0.21
	#2	-0.28	-0.07
	#3	-0.13	-0.21
Bi(OTf) ₃	#1	0.03	0.27
	#2	-0.26	0.08
	#3	0.10	0.25
Al(OTf) ₃	#1	-0.28	-0.04
	#2	-0.29	-0.09
	#3	-0.29	0.07
In(OTf) ₃	#1	-0.24	0.01
	#2	-0.28	0.11
	#3	-0.25	0.00
Dy(OTf) ₃	#1	-0.27	-0.16
	#2	-0.28	-0.09
	#3	-0.18	0.21
Ce(OTf) ₃	#1	-0.25	-0.19
	#2	-0.05	-0.27
	#3	-0.12	-0.25
no triflate	#1	0.12	-0.30
	#2	0.16	-0.29
	#3	0.16	-0.26

Figure S5. PCA on α_1 , for R is measured at different time interval [40s;49s] | a, PCA scores with 95% confidence ellipsoids. b, Individual variance for the different PC. c, PCA loadings of the different sensing elements' response for PC1 and PC2.

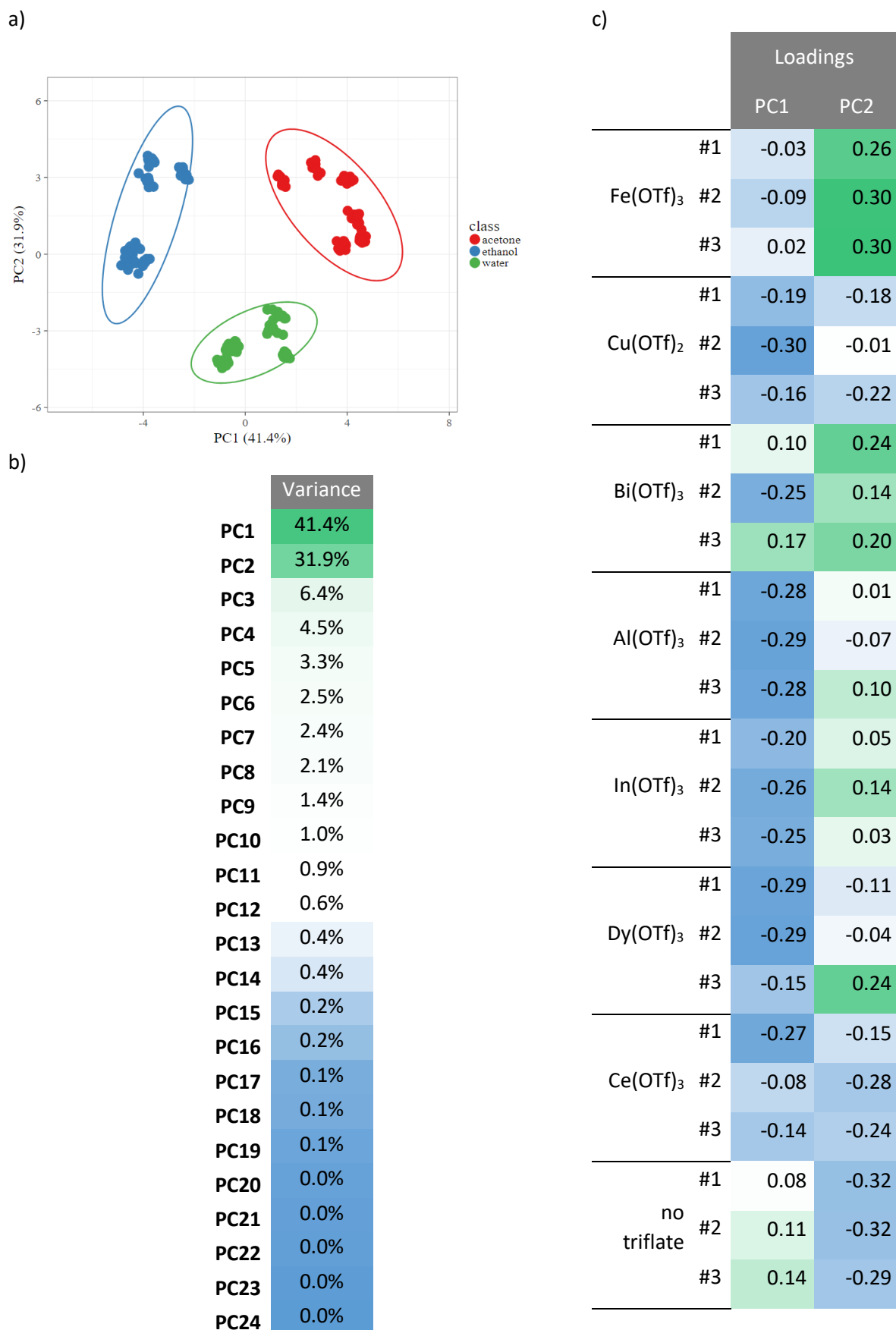
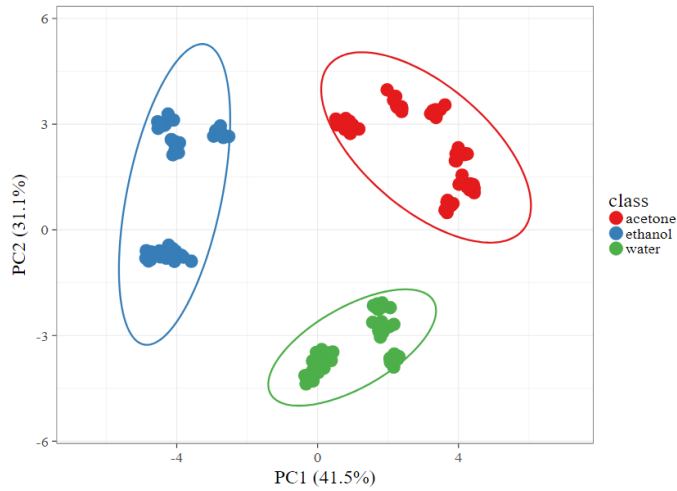


Figure S6. PCA on α_1 , for R is measured at different time interval [50s;59s] | a, PCA scores with 95% confidence ellipsoids. b, Individual variance for the different PC. c, PCA loadings of the different sensing elements' response for PC1 and PC2.

a)



b)

	Variance
PC1	41.5%
PC2	31.1%
PC3	6.4%
PC4	5.0%
PC5	3.2%
PC6	2.8%
PC7	2.4%
PC8	2.3%
PC9	1.3%
PC10	1.1%
PC11	0.8%
PC12	0.5%
PC13	0.4%
PC14	0.3%
PC15	0.3%
PC16	0.2%
PC17	0.1%
PC18	0.1%
PC19	0.1%
PC20	0.1%
PC21	0.0%
PC22	0.0%
PC23	0.0%
PC24	0.0%

c)

		Loadings	
		PC1	PC2
Fe(OTf) ₃	#1	-0.01	-0.26
	#2	0.07	-0.30
	#3	-0.05	-0.29
Cu(OTf) ₂	#1	0.20	0.15
	#2	0.29	-0.05
	#3	0.17	0.21
Bi(OTf) ₃	#1	-0.16	-0.19
	#2	0.22	-0.20
	#3	-0.21	-0.15
Al(OTf) ₃	#1	0.28	-0.04
	#2	0.29	0.07
	#3	0.28	-0.11
In(OTf) ₃	#1	0.18	-0.08
	#2	0.25	-0.17
	#3	0.25	-0.05
Dy(OTf) ₃	#1	0.30	0.06
	#2	0.29	0.01
	#3	0.13	-0.25
Ce(OTf) ₃	#1	0.28	0.13
	#2	0.10	0.27
	#3	0.16	0.24
no triflate	#1	-0.04	0.34
	#2	-0.08	0.33
	#3	-0.10	0.32

Figure S7. PCA on α_1 , for R is measured at different time interval [60s;69s] | **a**, PCA scores with 95% confidence ellipsoids. **b**, Individual variance for the different PC. **c**, PCA loadings of the different sensing elements' response for PC1 and PC2.

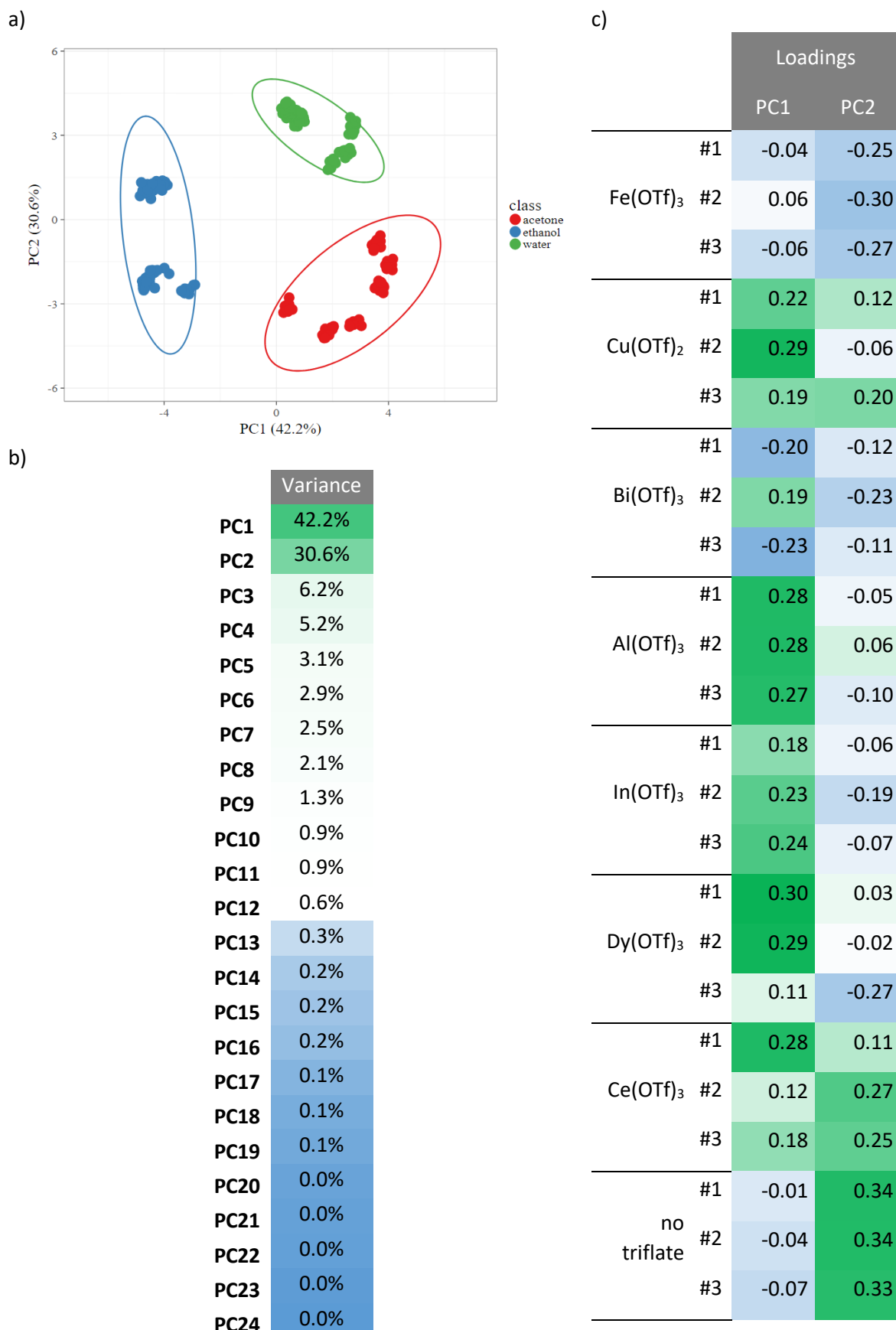


Figure S8. PCA on α_1 , for R is measured at different time interval [70s;79s] | a, PCA scores with 95% confidence ellipsoids. b, Individual variance for the different PC. c, PCA loadings of the different sensing elements' response for PC1 and PC2.

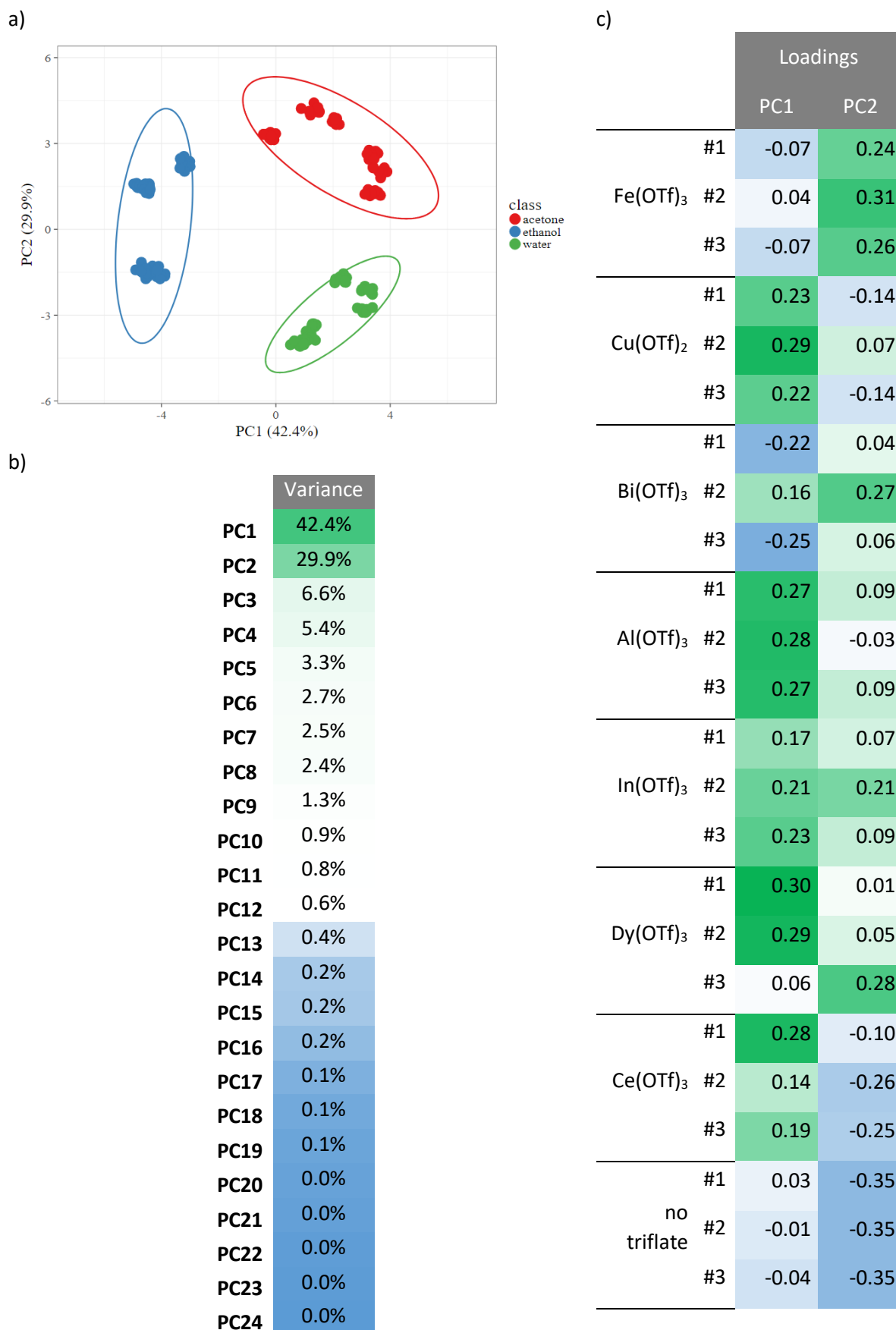
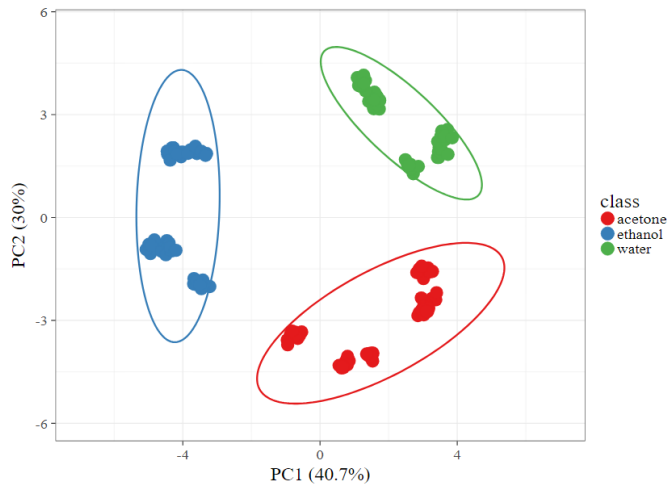


Figure S9. PCA on α_1 , for R is measured at different time interval [80s;89s] | **a**, PCA scores with 95% confidence ellipsoids. **b**, Individual variance for the different PC. **c**, PCA loadings of the different sensing elements' response for PC1 and PC2.

a)



b)

	Variance
PC1	40.7%
PC2	30.0%
PC3	6.9%
PC4	5.9%
PC5	3.7%
PC6	3.0%
PC7	2.8%
PC8	2.3%
PC9	1.1%
PC10	0.9%
PC11	0.7%
PC12	0.5%
PC13	0.4%
PC14	0.3%
PC15	0.2%
PC16	0.2%
PC17	0.1%
PC18	0.1%
PC19	0.1%
PC20	0.0%
PC21	0.0%
PC22	0.0%
PC23	0.0%
PC24	0.0%

c)

		Loadings	
		PC1	PC2
Fe(OTf) ₃	#1	-0.11	0.22
	#2	0.02	0.30
	#3	-0.08	0.24
Cu(OTf) ₂	#1	0.23	-0.11
	#2	0.28	0.10
	#3	0.20	-0.16
Bi(OTf) ₃	#1	-0.22	-0.04
	#2	0.14	0.29
	#3	-0.26	0.01
Al(OTf) ₃	#1	0.26	0.11
	#2	0.28	-0.02
	#3	0.27	0.08
In(OTf) ₃	#1	0.15	0.06
	#2	0.18	0.24
	#3	0.22	0.11
Dy(OTf) ₃	#1	0.30	0.05
	#2	0.29	0.09
	#3	0.03	0.29
Ce(OTf) ₃	#1	0.29	-0.08
	#2	0.16	-0.24
	#3	0.22	-0.23
no triflate	#1	0.05	-0.35
	#2	0.04	-0.35
	#3	0.01	-0.35

Figure S10. PCA on α_1 , for R is measured at different time interval [90s;99s] | a, PCA scores with 95% confidence ellipsoids. b, Individual variance for the different PC. c, PCA loadings of the different sensing elements' response for PC1 and PC2.

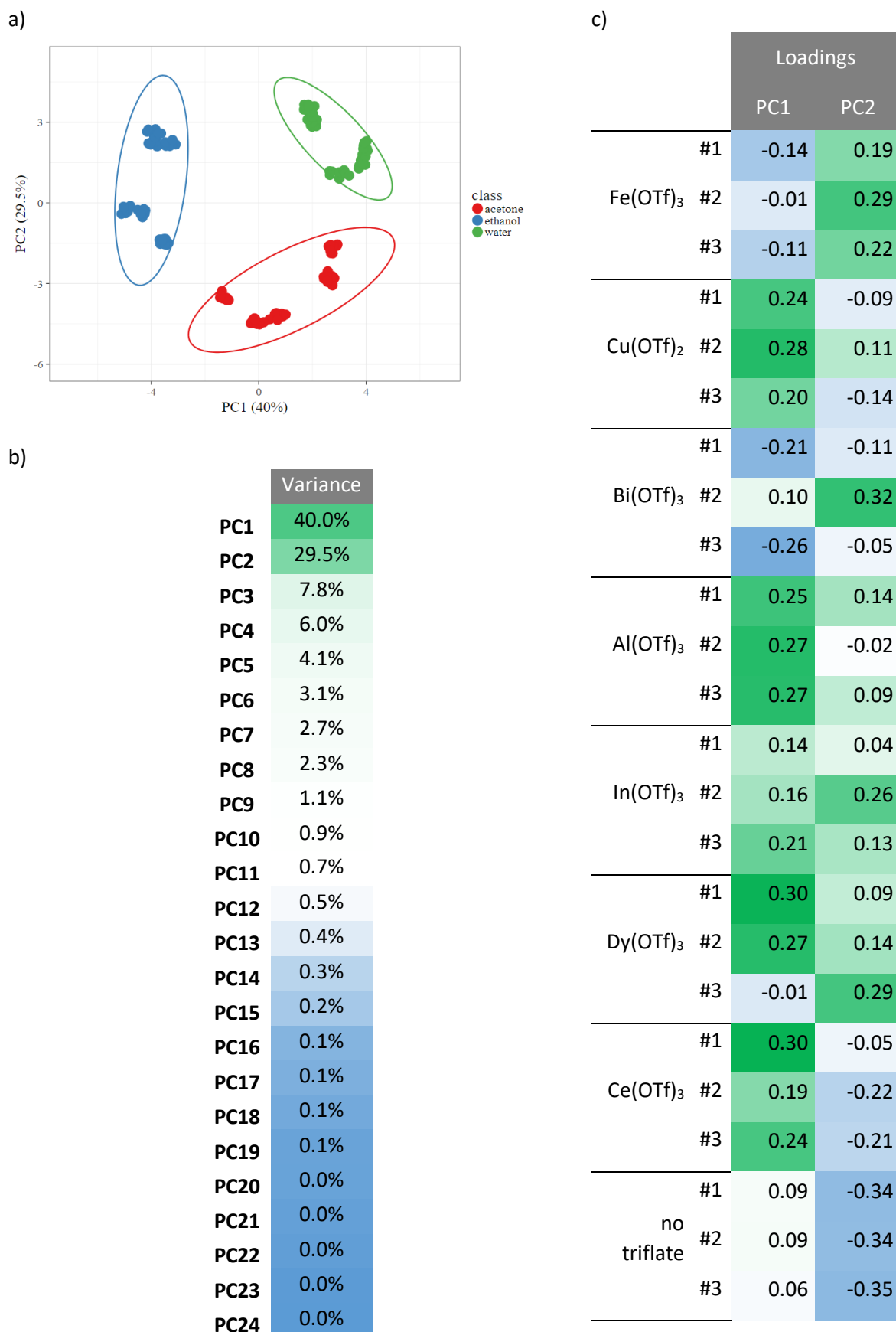


Figure S11. PCA on α_1 , for R is measured at different time interval [100s;109s] | a, PCA scores with 95% confidence ellipsoids. b, Individual variance for the different PC. c, PCA loadings of the different sensing elements' response for PC1 and PC2.

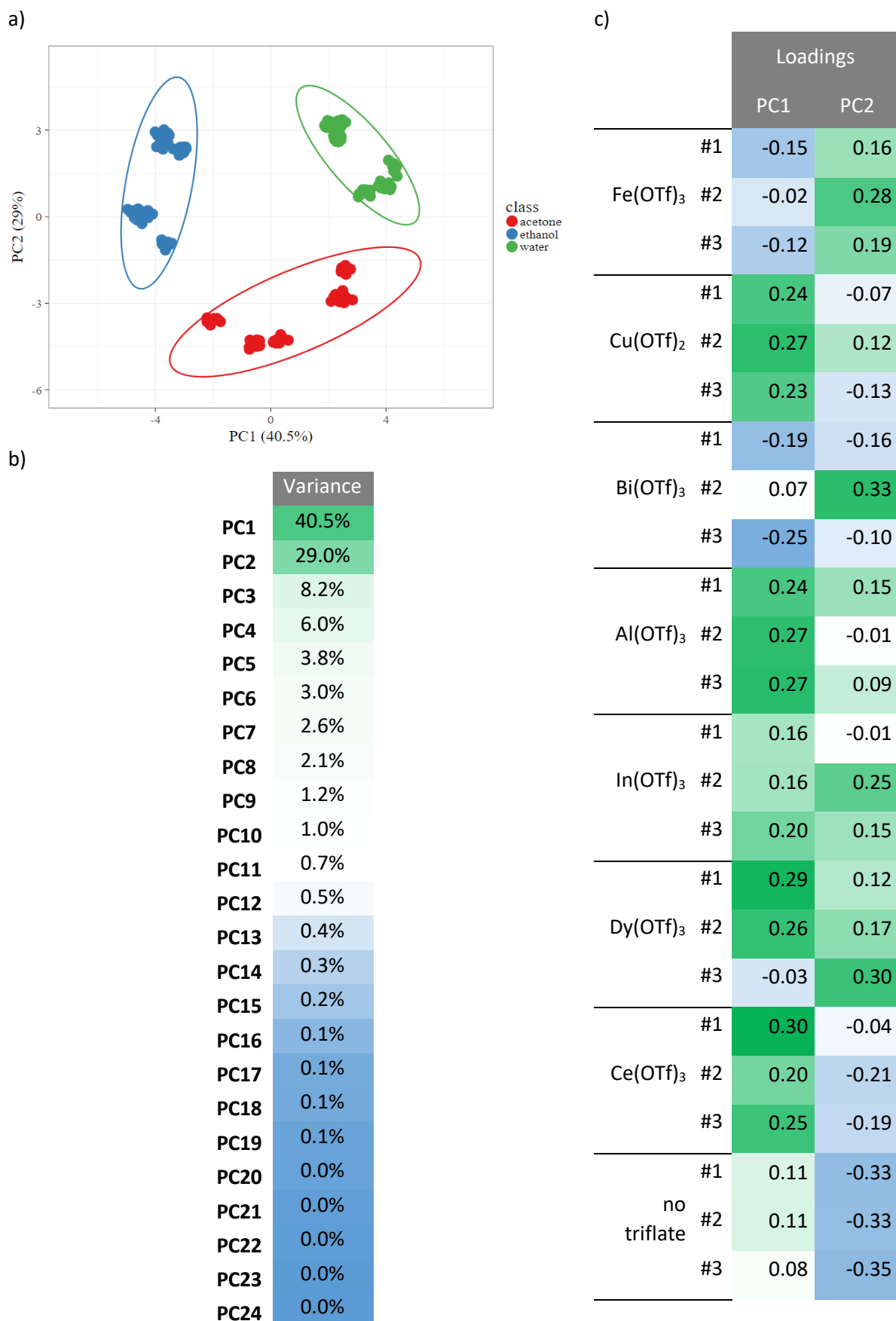


Figure S12. PCA on α_1 , for R is measured at different time interval [110s;119s] | a, PCA scores with 95% confidence ellipsoids. b, Individual variance for the different PC. c, PCA loadings of the different sensing elements' response for PC1 and PC2.

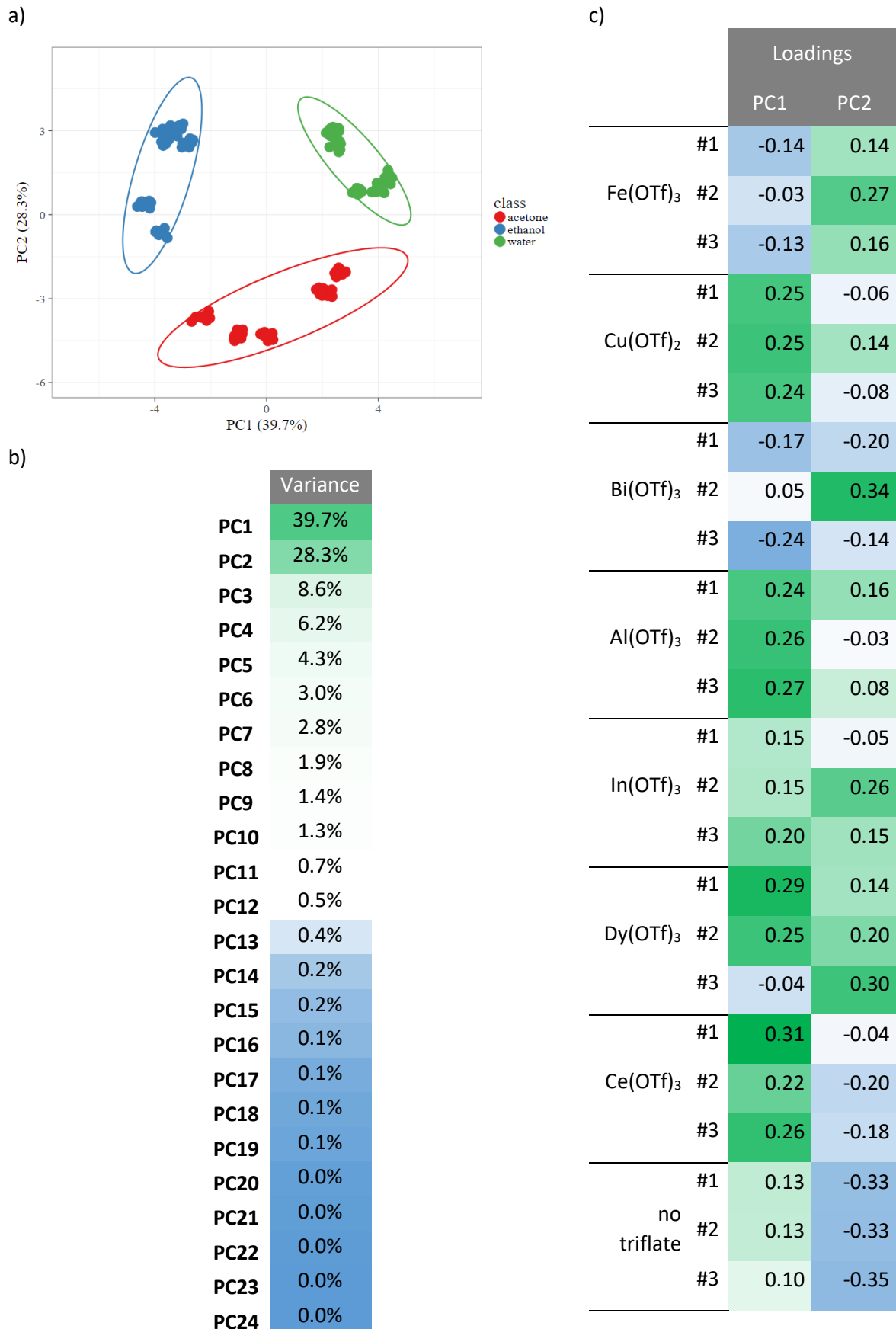


Figure S13. PCA on α_1 , for R is measured at different time interval [120s;129s] | a, PCA scores with 95% confidence ellipsoids. b, Individual variance for the different PC. c, PCA loadings of the different sensing elements' response for PC1 and PC2.

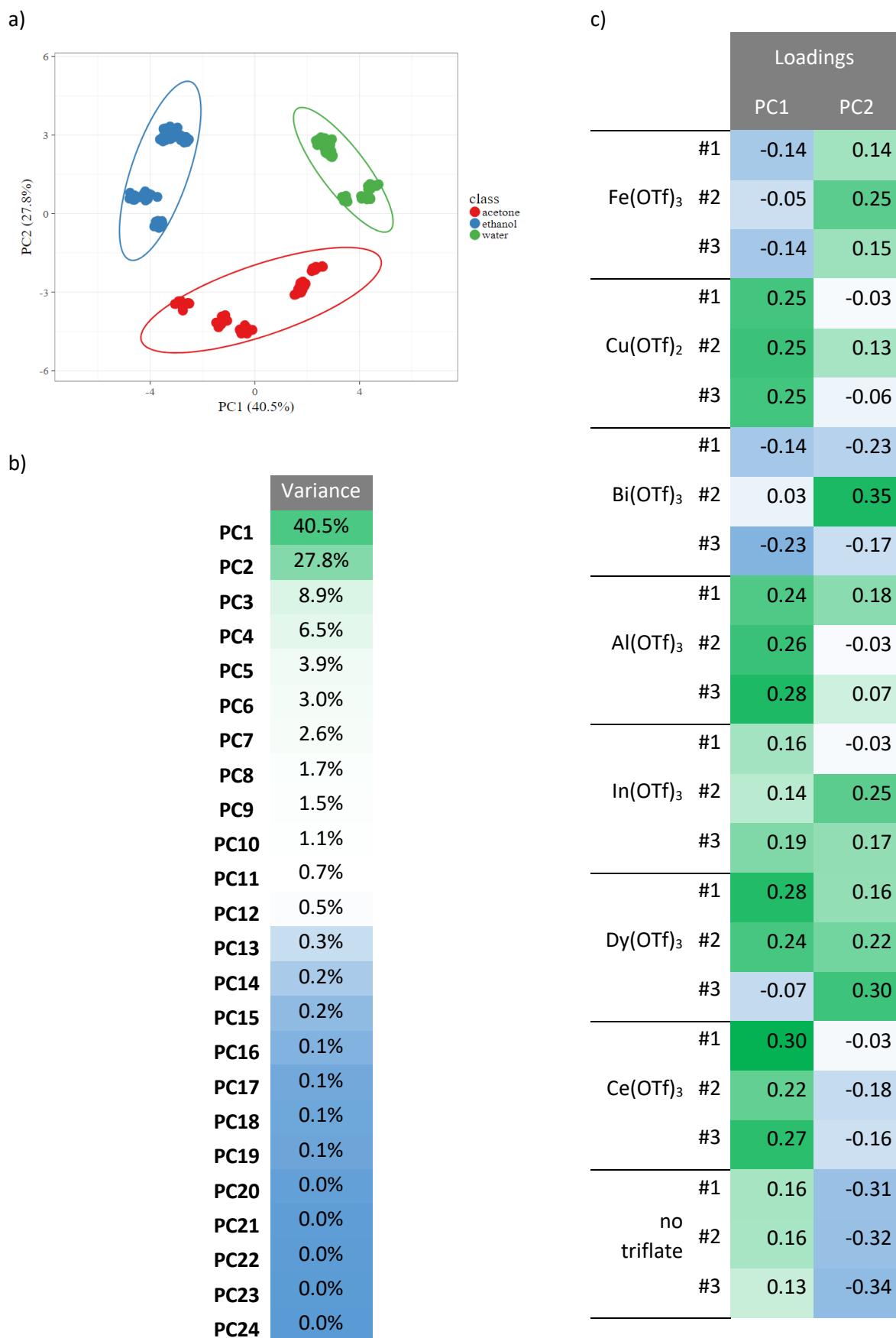


Figure S14. PCA on α_1 , for R is measured at different time interval [130s;139s] | a, PCA scores with 95% confidence ellipsoids. b, Individual variance for the different PC. c, PCA loadings of the different sensing elements' response for PC1 and PC2.

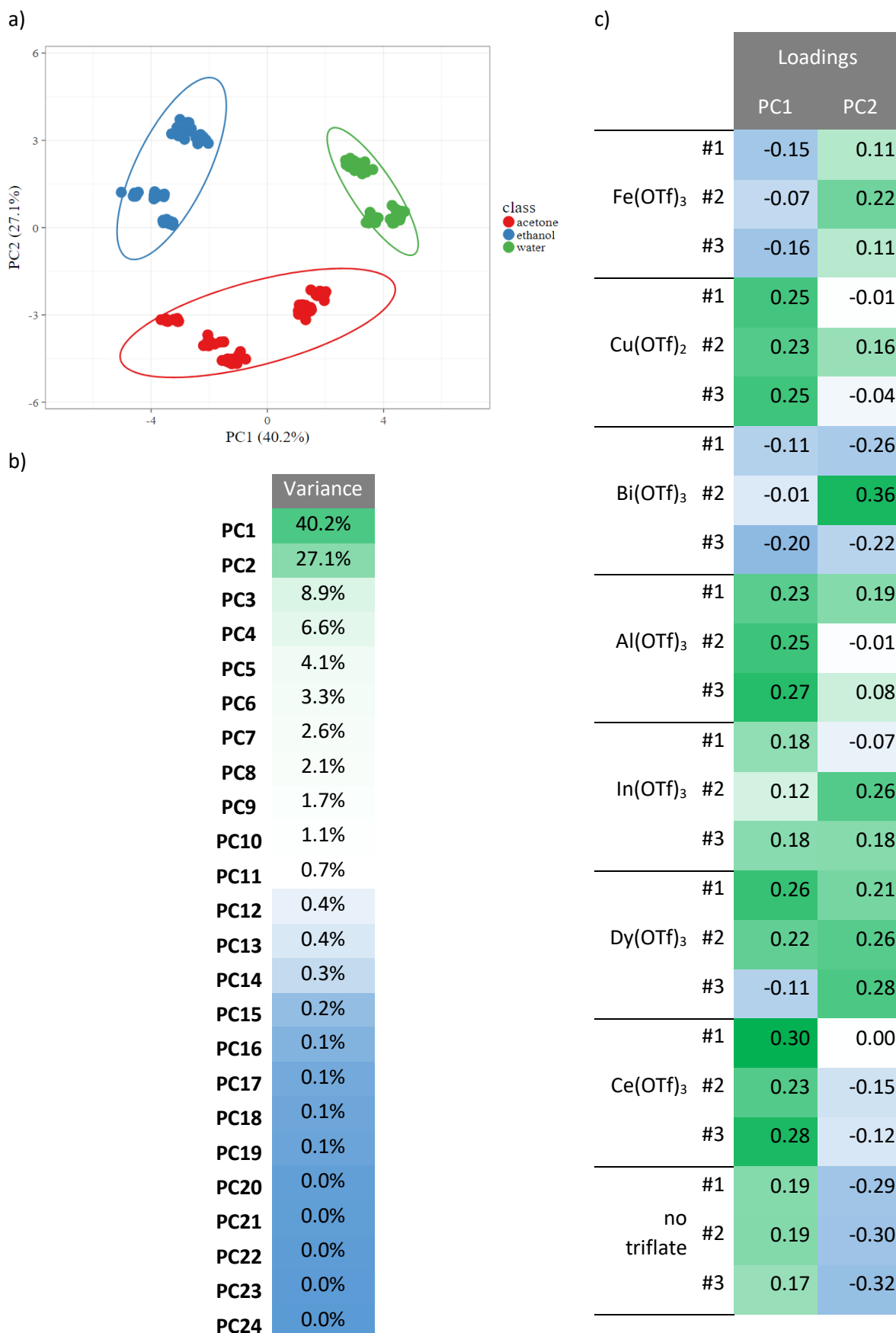


Figure S15. PCA on α_1 , for R is measured at different time interval [140s;149s] | a, PCA scores with 95% confidence ellipsoids. b, Individual variance for the different PC. c, PCA loadings of the different sensing elements' response for PC1 and PC2.

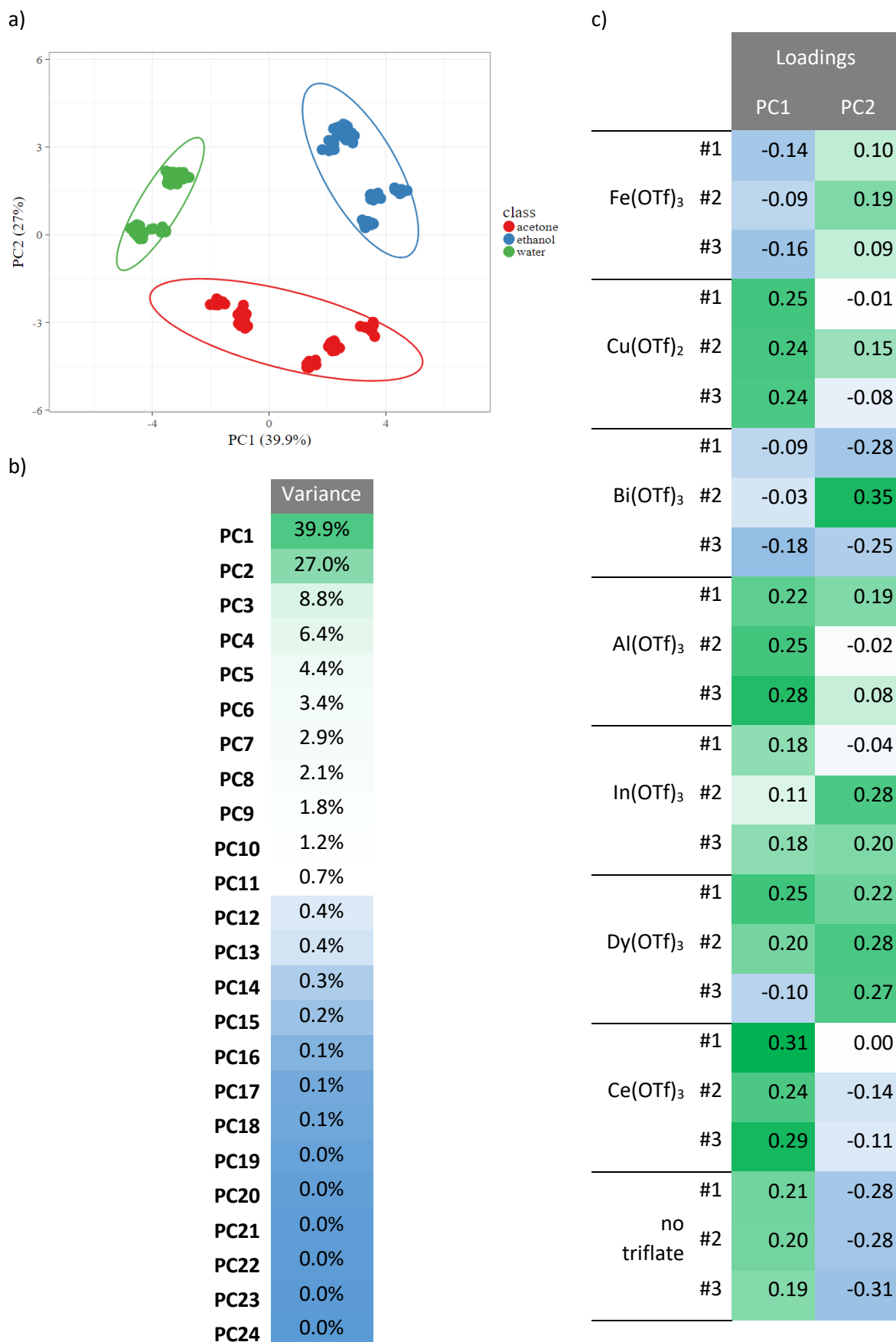


Figure S16. PCA on α_1 , for R is measured at different time interval [150s;159s] | a, PCA scores with 95% confidence ellipsoids. b, Individual variance for the different PC. c, PCA loadings of the different sensing elements' response for PC1 and PC2.

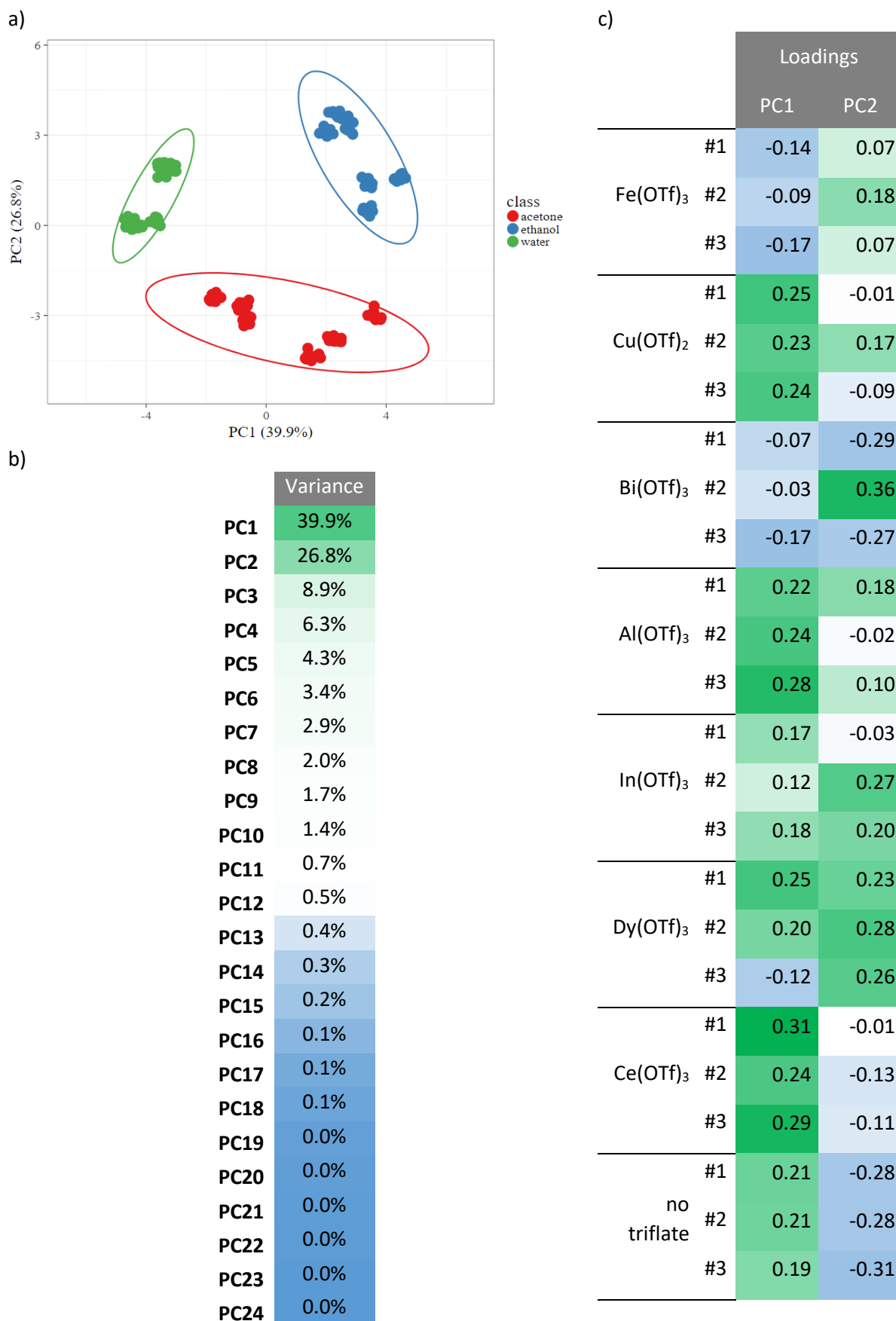


Figure S17. PCA on α_1 , for R is measured at different time interval [160s;169s] | a, PCA scores with 95% confidence ellipsoids. b, Individual variance for the different PC. c, PCA loadings of the different sensing elements' response for PC1 and PC2.

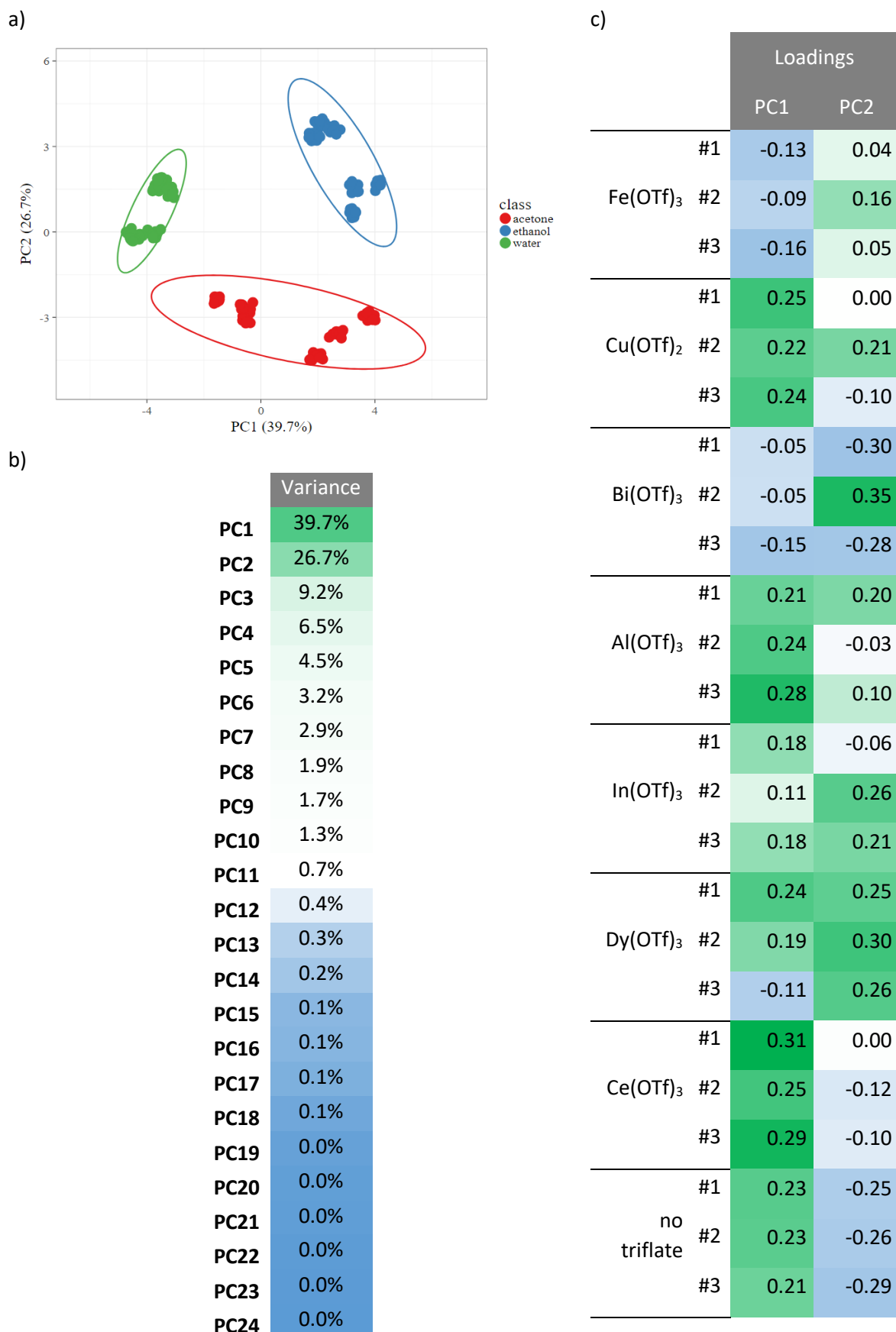


Figure S18. PCA on α_1 , for R is measured at different time interval [170s;179s] | a, PCA scores with 95% confidence ellipsoids. b, Individual variance for the different PC. c, PCA loadings of the different sensing elements' response for PC1 and PC2.

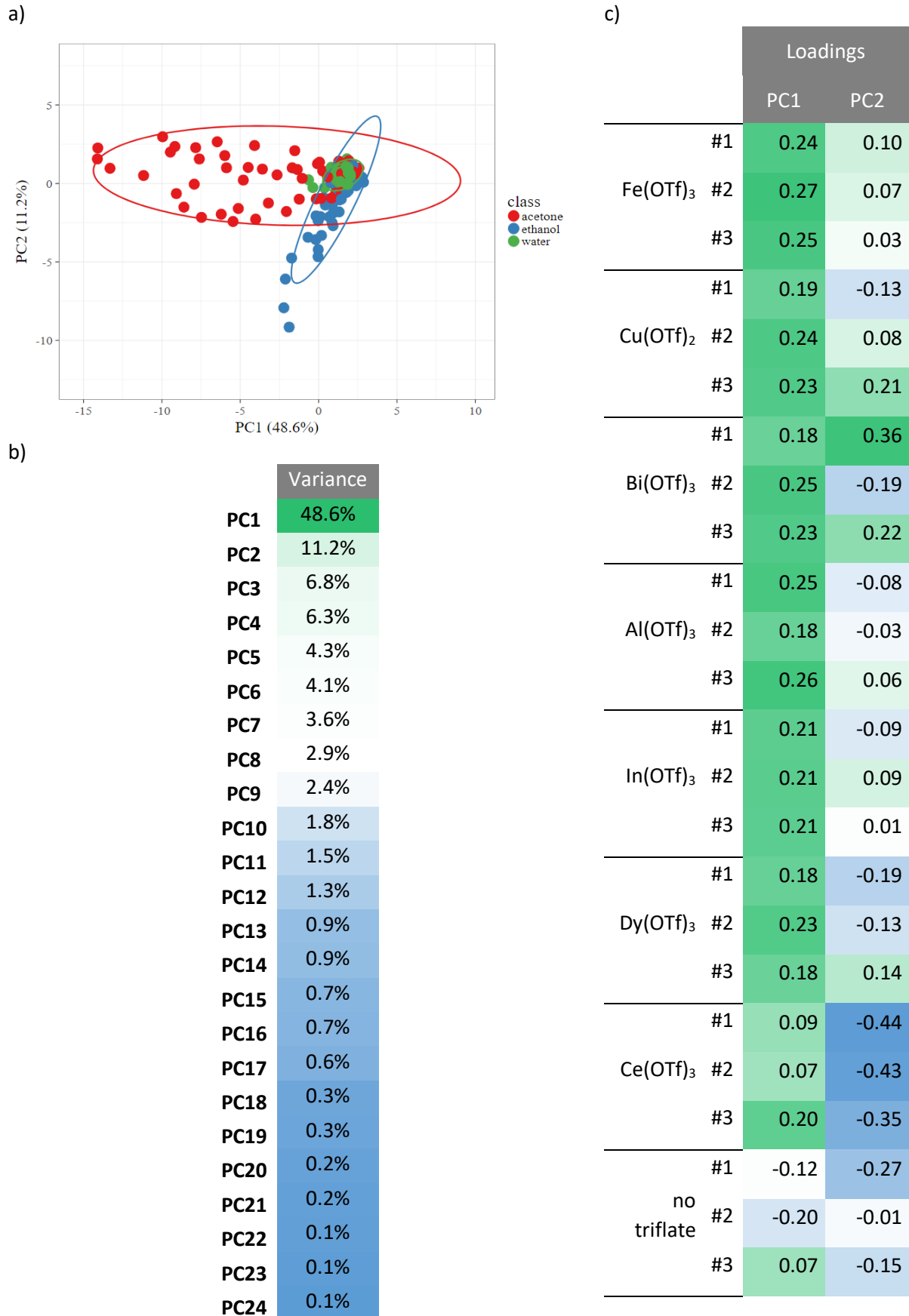


Figure S19. PCA on α_2 , for R is measured at different time interval [1s;9s] | a, PCA scores with 95% confidence ellipsoids. b, Individual variance for the different PC. c, PCA loadings of the different sensing elements' response for PC1 and PC2.

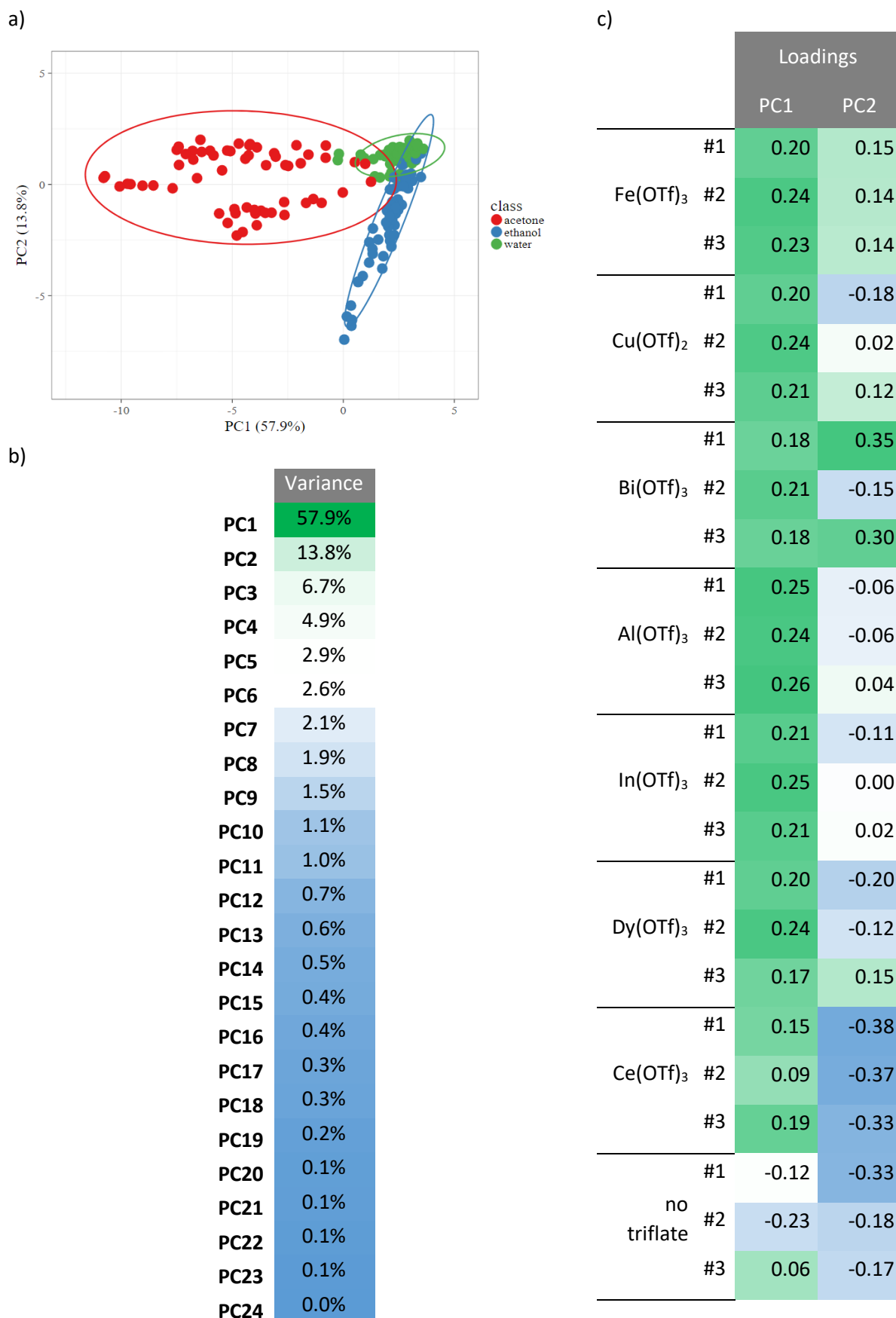


Figure S20. PCA on α_2 , for R is measured at different time interval [10s;19s] | a, PCA scores with 95% confidence ellipsoids. b, Individual variance for the different PC. c, PCA loadings of the different sensing elements' response for PC1 and PC2.

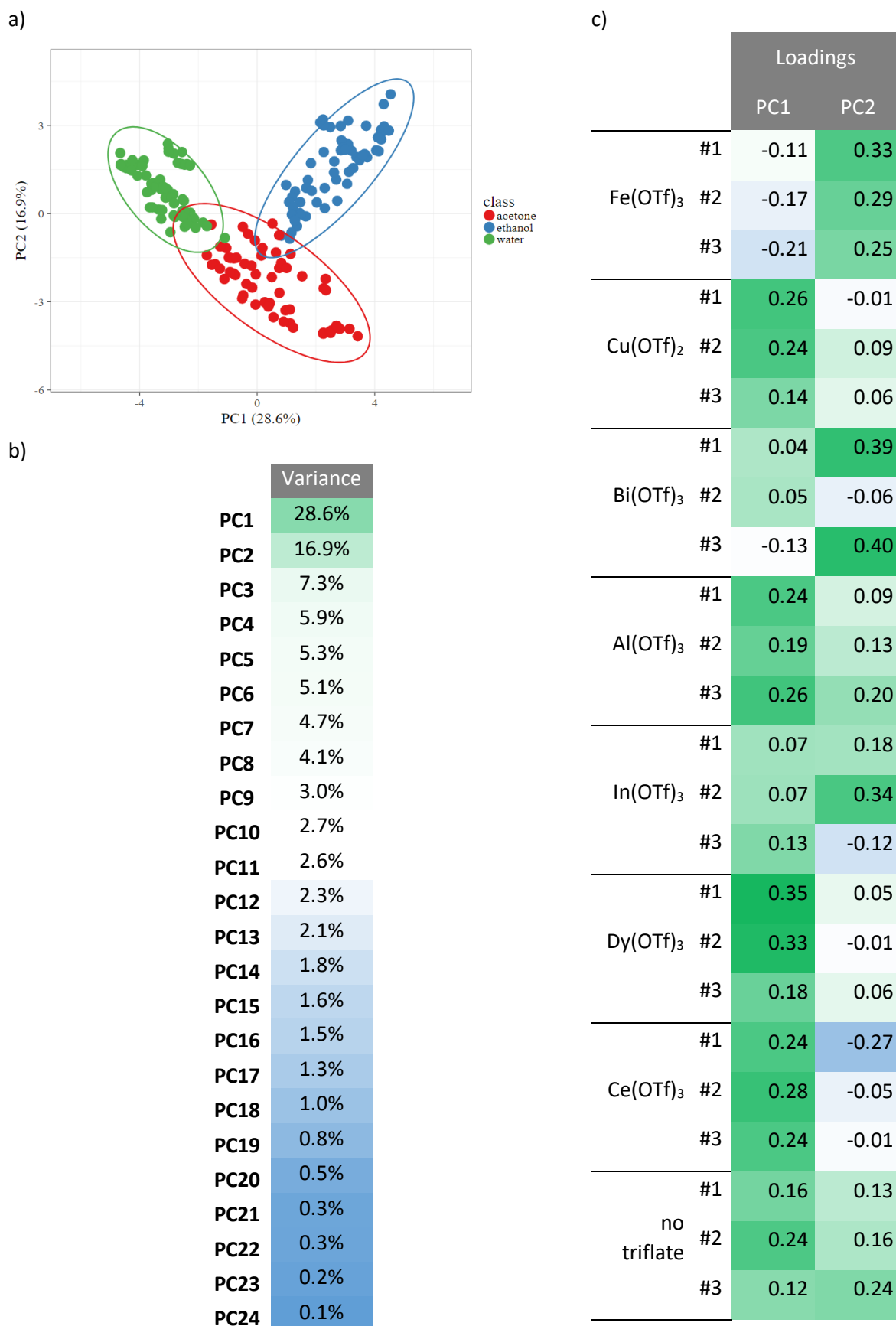


Figure S21. PCA on α_2 , for R is measured at different time interval [20s;29s] | a, PCA scores with 95% confidence ellipsoids. b, Individual variance for the different PC. c, PCA loadings of the different sensing elements' response for PC1 and PC2.

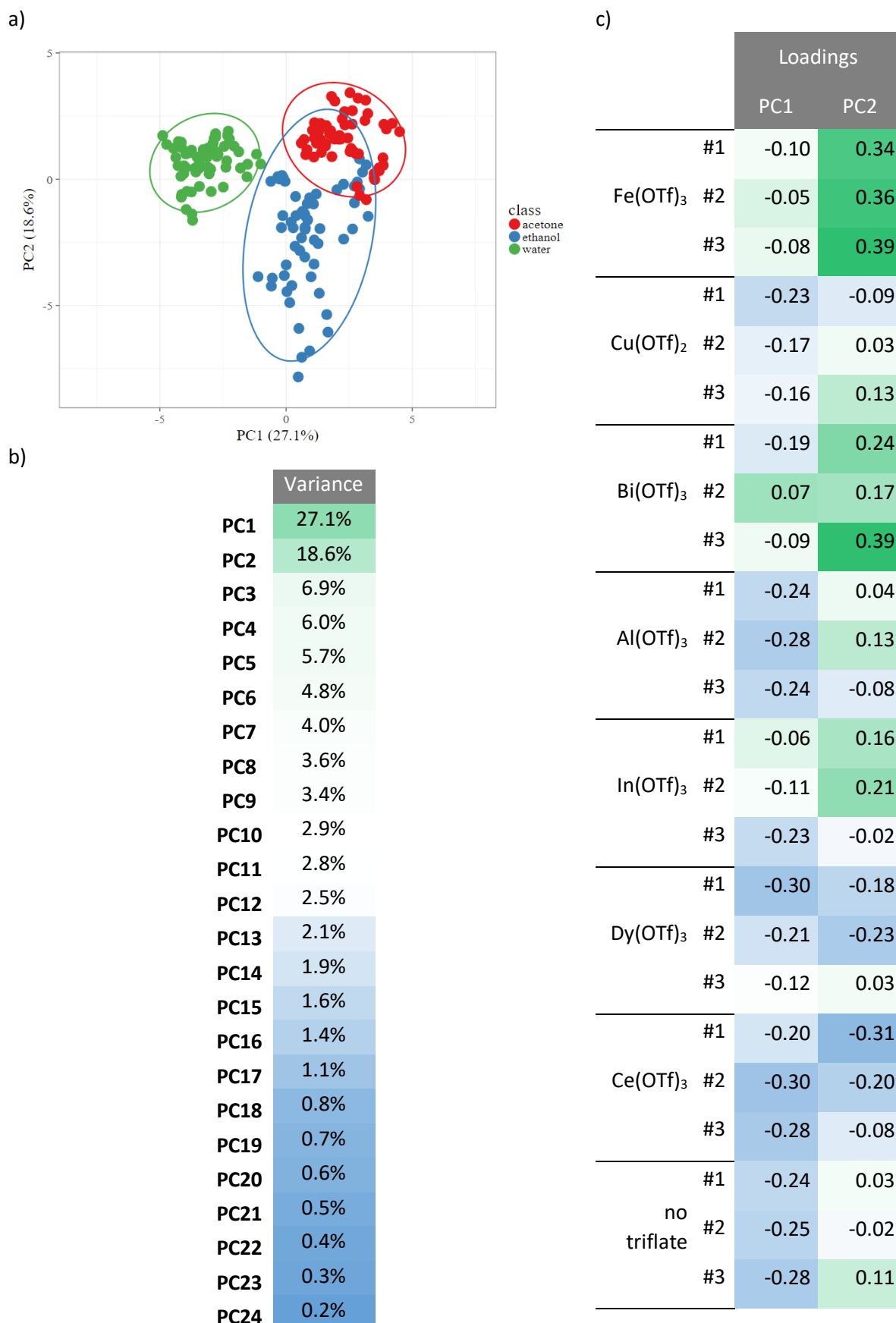


Figure S22. PCA on α_2 , for R is measured at different time interval [30s;39s] | a, PCA scores with 95% confidence ellipsoids. b, Individual variance for the different PC. c, PCA loadings of the different sensing elements' response for PC1 and PC2.

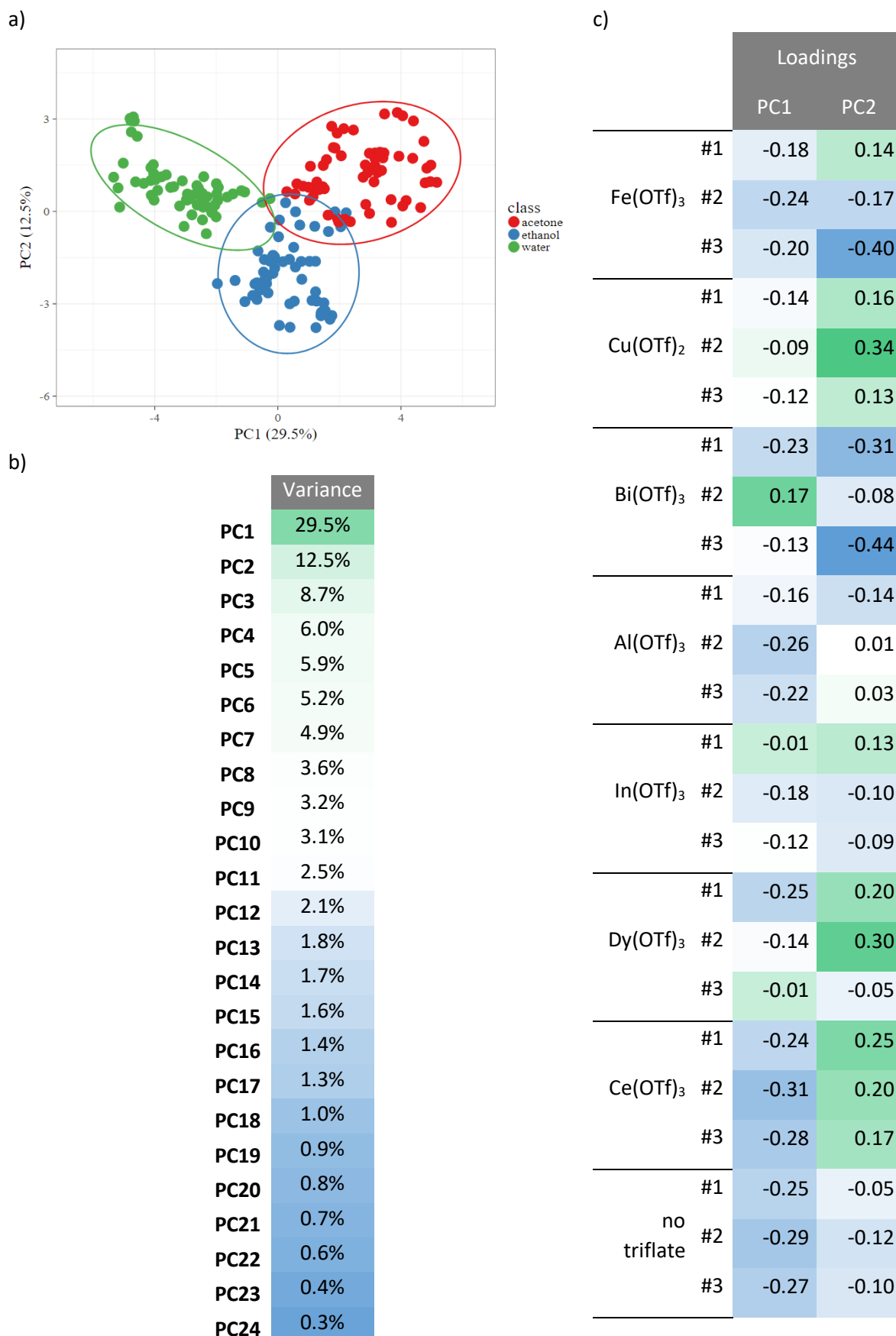


Figure S23. PCA on α_2 , for R is measured at different time interval [40s;49s] | a, PCA scores with 95% confidence ellipsoids. b, Individual variance for the different PC. c, PCA loadings of the different sensing elements' response for PC1 and PC2.

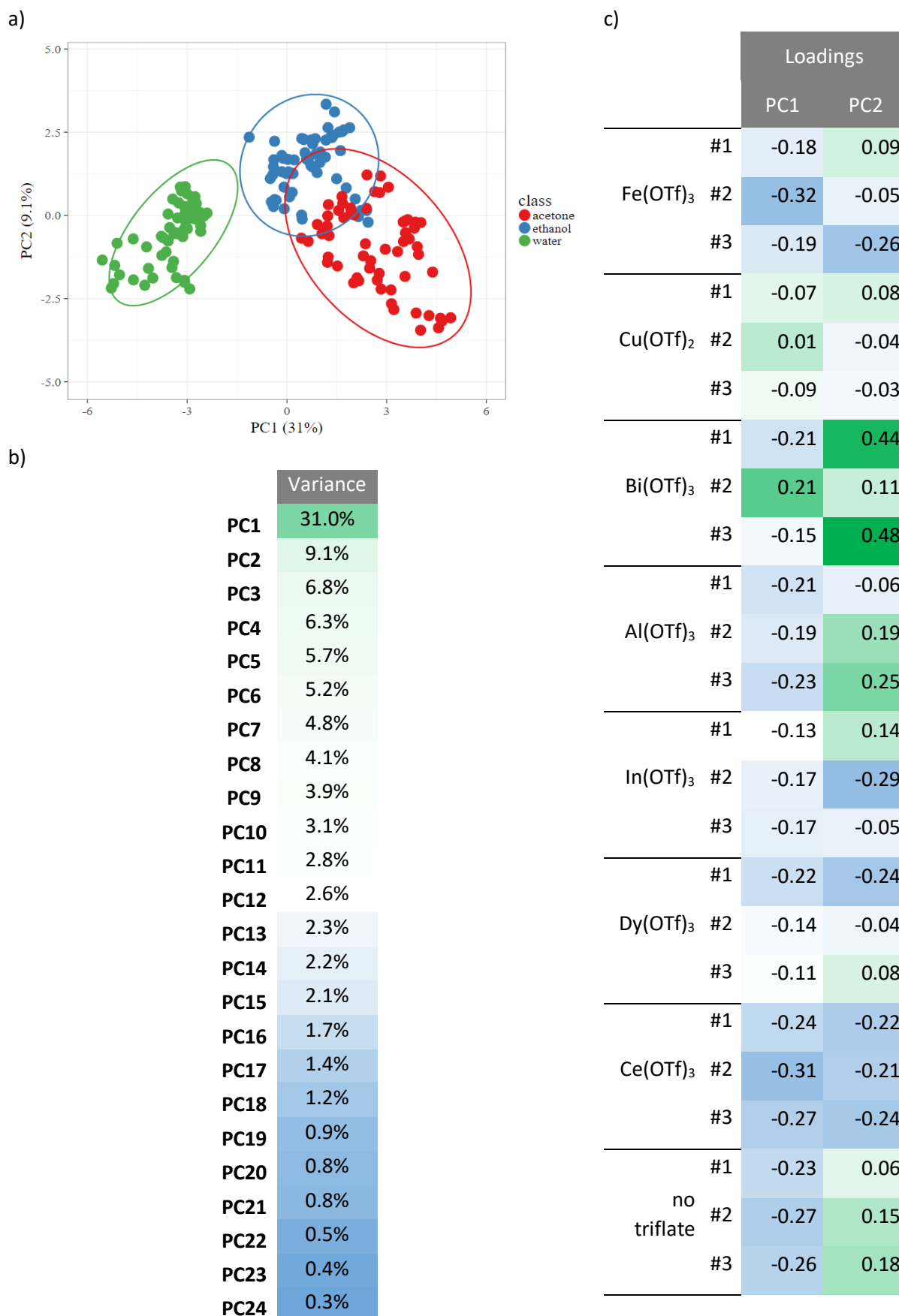


Figure S24. PCA on α_2 , for R is measured at different time interval [50s;59s] | a, PCA scores with 95% confidence ellipsoids. b, Individual variance for the different PC. c, PCA loadings of the different sensing elements' response for PC1 and PC2.

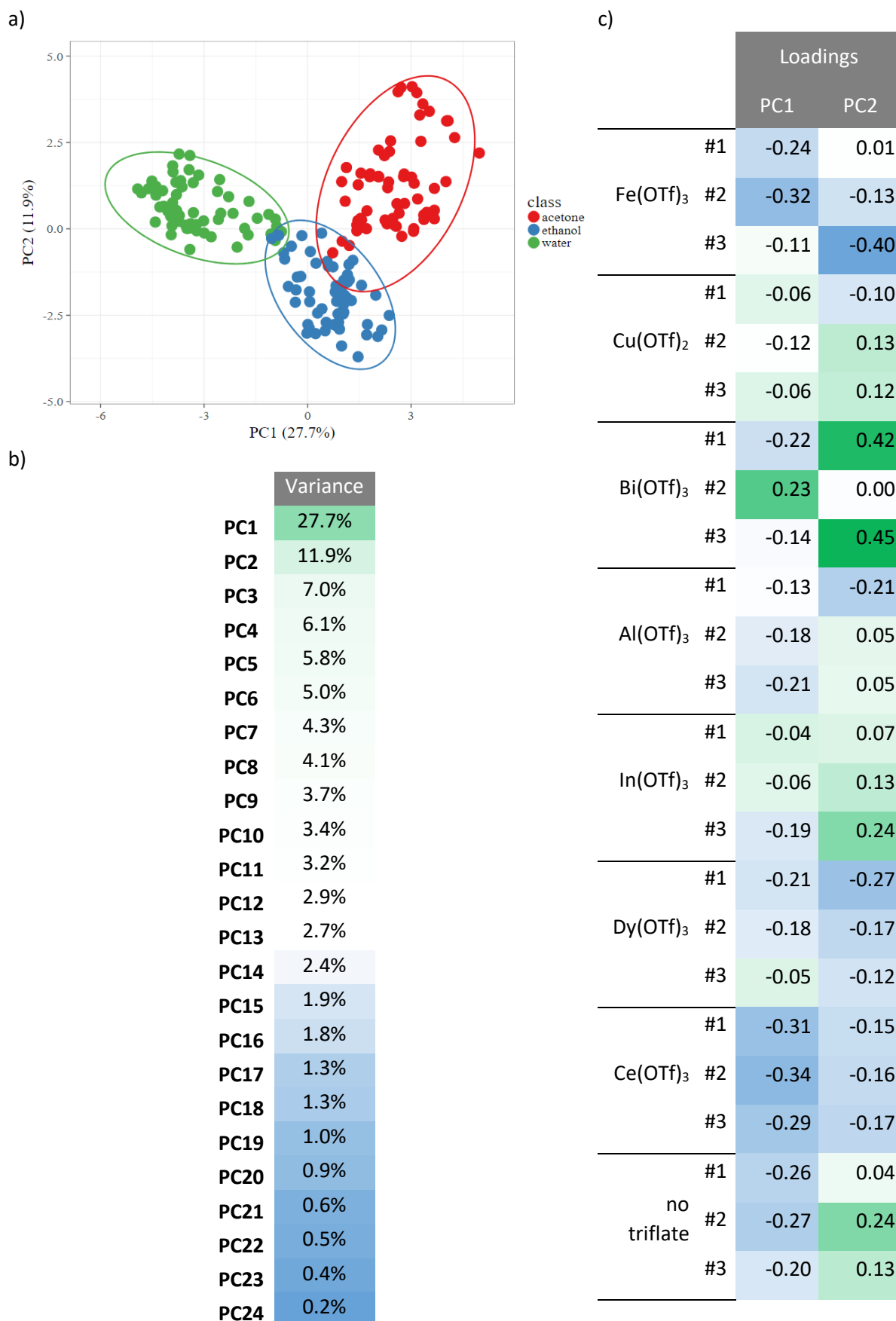


Figure S25. PCA on α_2 , for R is measured at different time interval [60s;69s] | a, PCA scores with 95% confidence ellipsoids. b, Individual variance for the different PC. c, PCA loadings of the different sensing elements' response for PC1 and PC2.

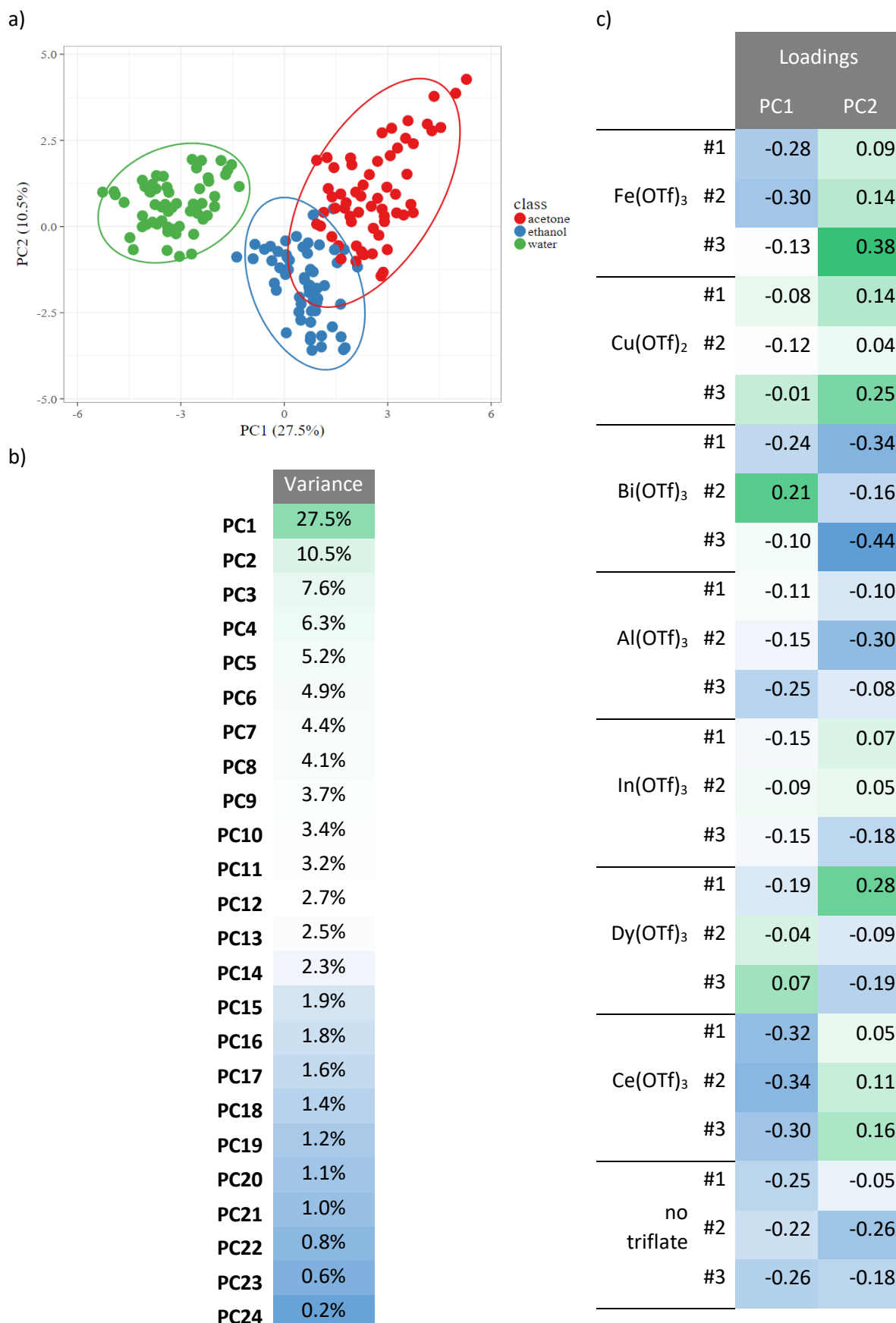


Figure S26. PCA on α_2 , for R is measured at different time interval [70s;79s] | a, PCA scores with 95% confidence ellipsoids. b, Individual variance for the different PC. c, PCA loadings of the different sensing elements' response for PC1 and PC2.

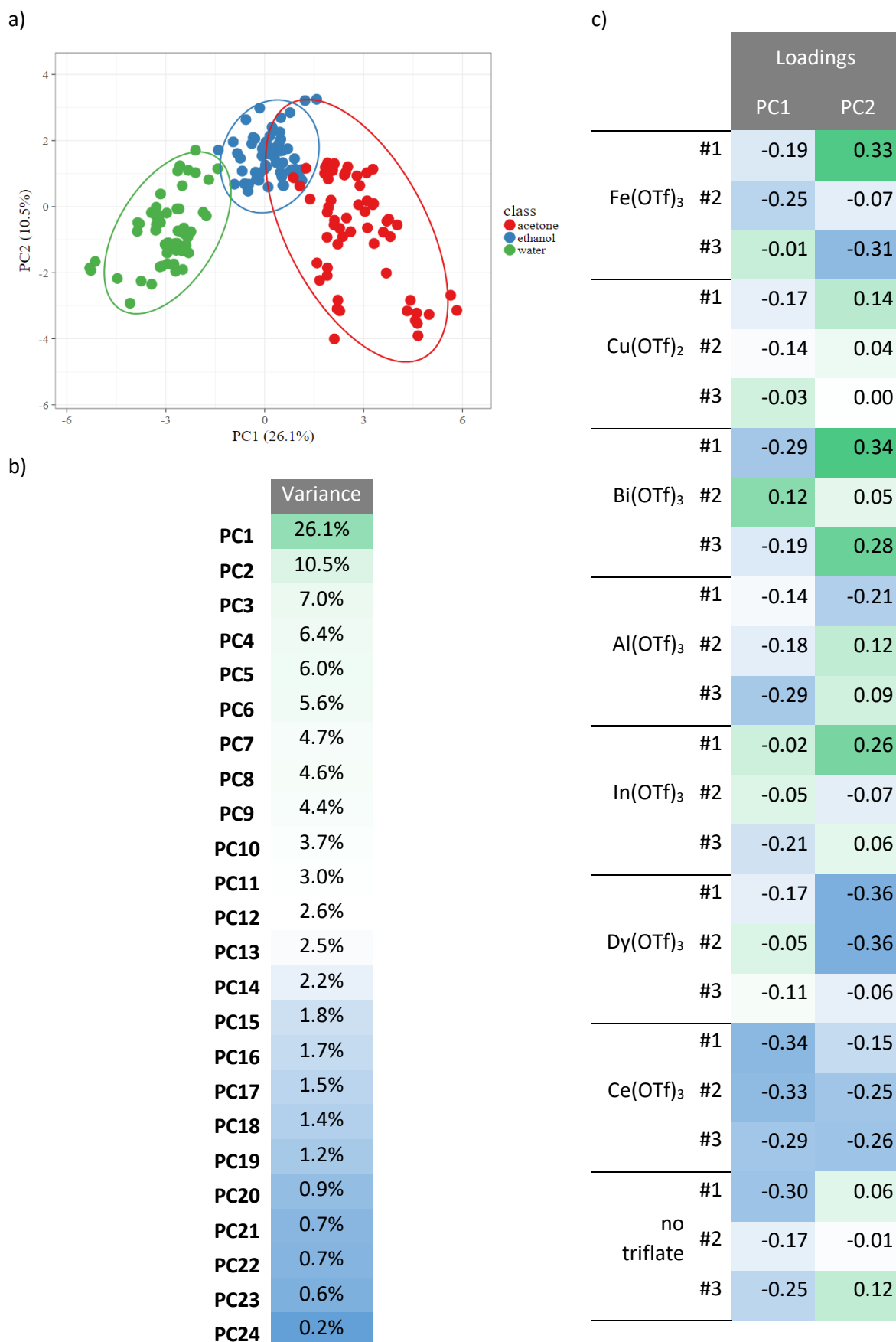


Figure S27. PCA on α_2 , for R is measured at different time interval [80s;89s] | a, PCA scores with 95% confidence ellipsoids. b, Individual variance for the different PC. c, PCA loadings of the different sensing elements' response for PC1 and PC2.

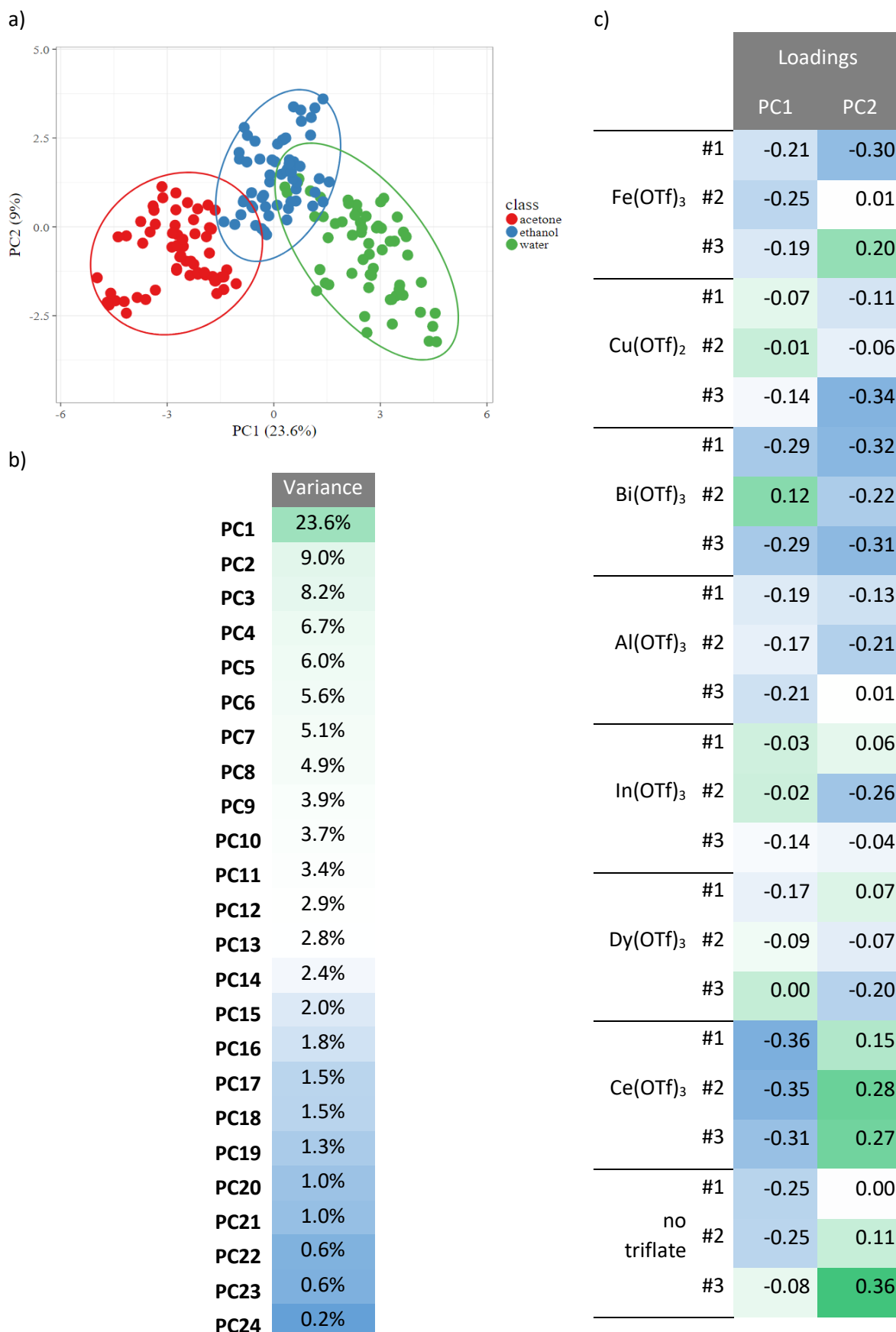


Figure S28. PCA on α_2 , for R is measured at different time interval [90s;99s] | a, PCA scores with 95% confidence ellipsoids. b, Individual variance for the different PC. c, PCA loadings of the different sensing elements' response for PC1 and PC2.

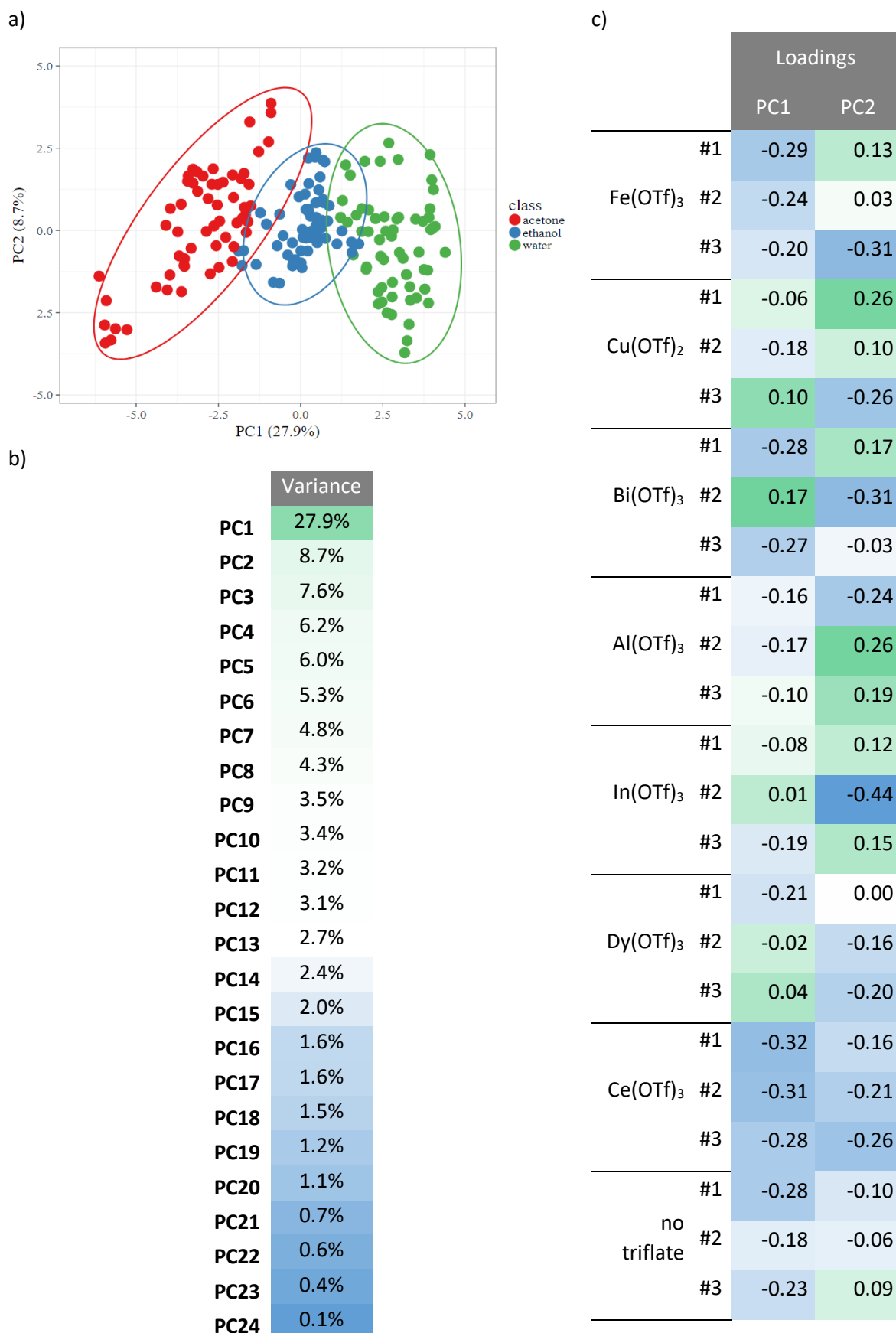


Figure S29. PCA on α_2 , for R is measured at different time interval [100s;109s] | a, PCA scores with 95% confidence ellipsoids. b, Individual variance for the different PC. c, PCA loadings of the different sensing elements' response for PC1 and PC2.

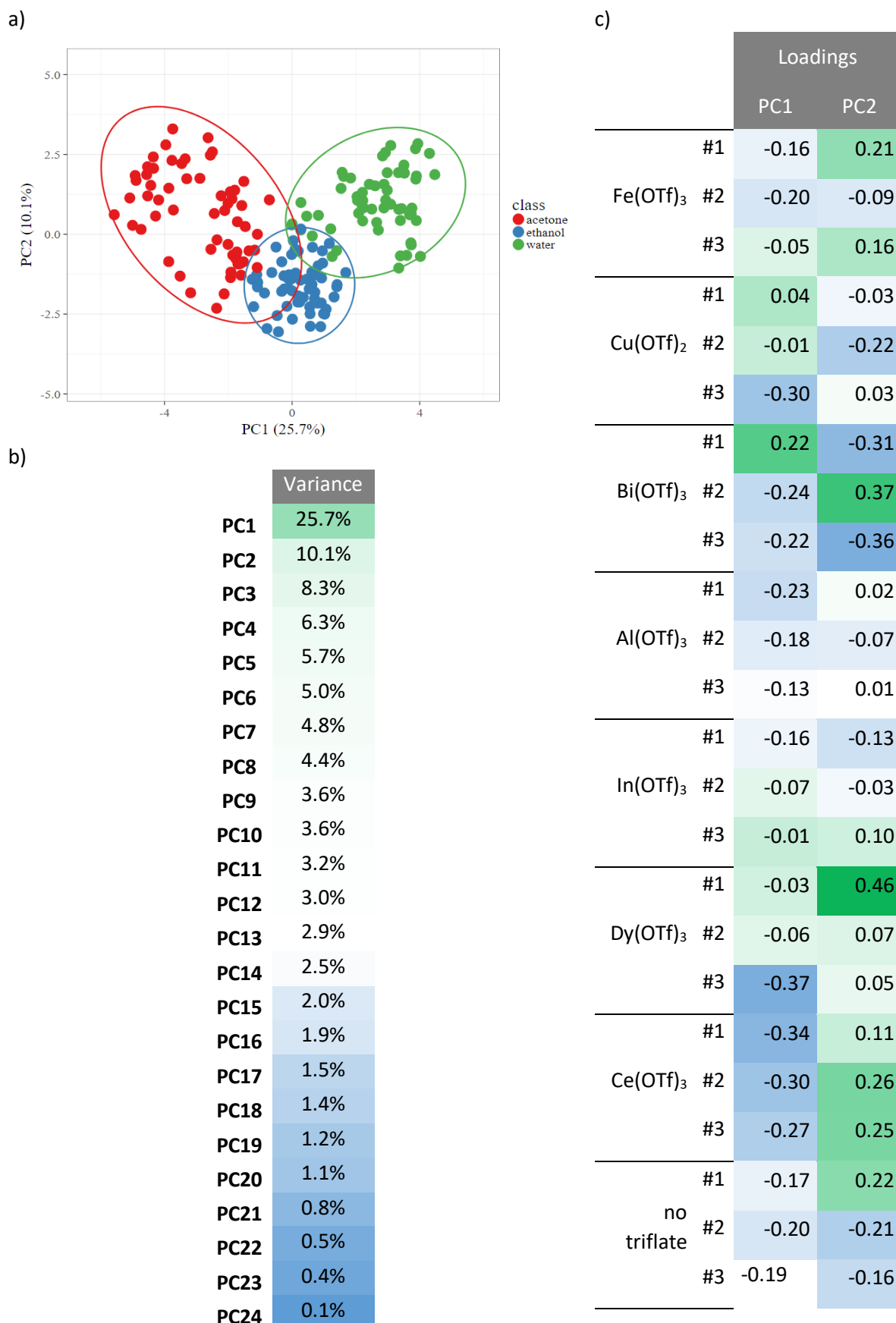


Figure S30. PCA on α_2 , for R is measured at different time interval [110s;119s] | a, PCA scores with 95% confidence ellipsoids. b, Individual variance for the different PC. c, PCA loadings of the different sensing elements' response for PC1 and PC2.

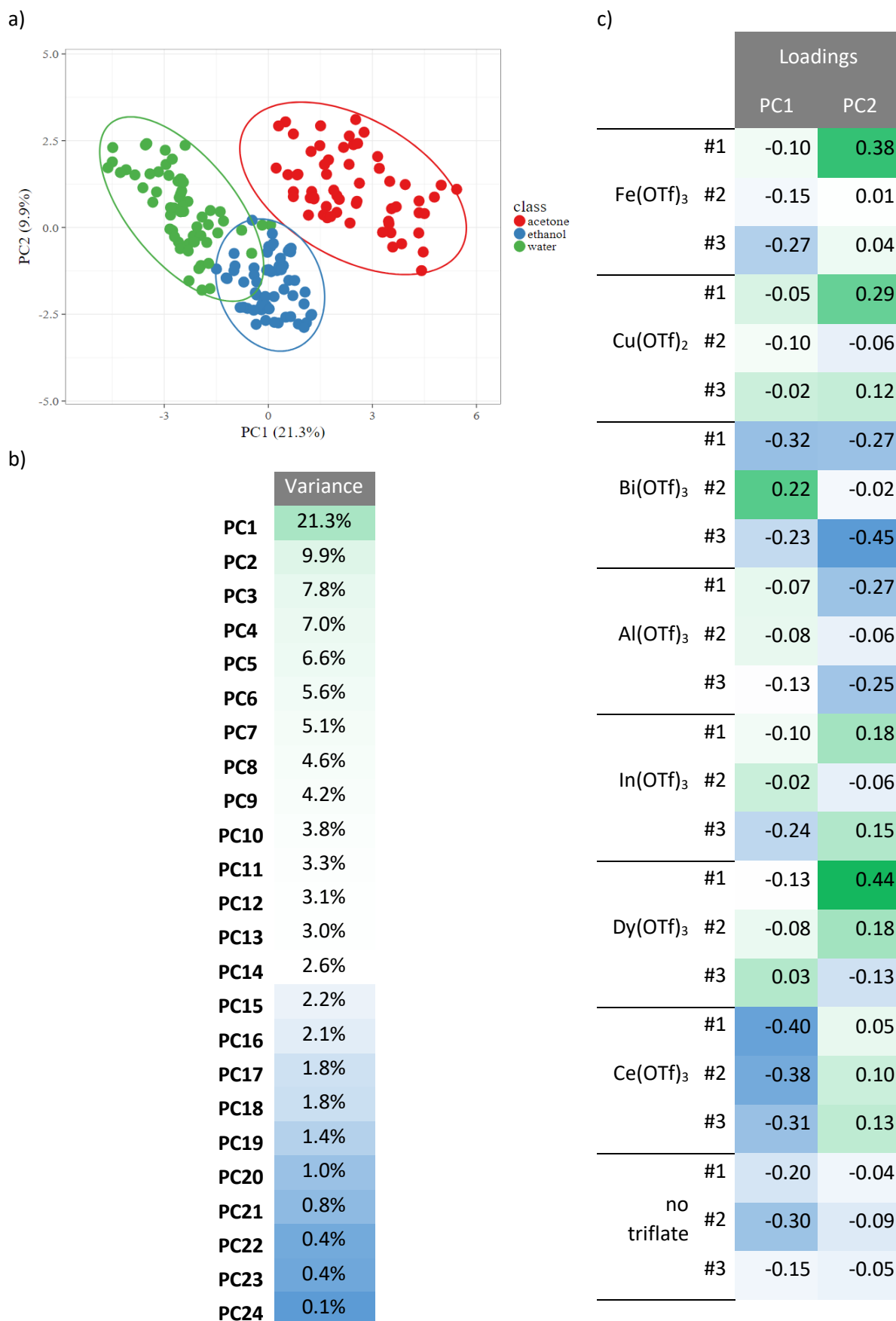


Figure S31. PCA on α_2 , for R is measured at different time interval [120s;129s] | a, PCA scores with 95% confidence ellipsoids. b, Individual variance for the different PC. c, PCA loadings of the different sensing elements' response for PC1 and PC2.

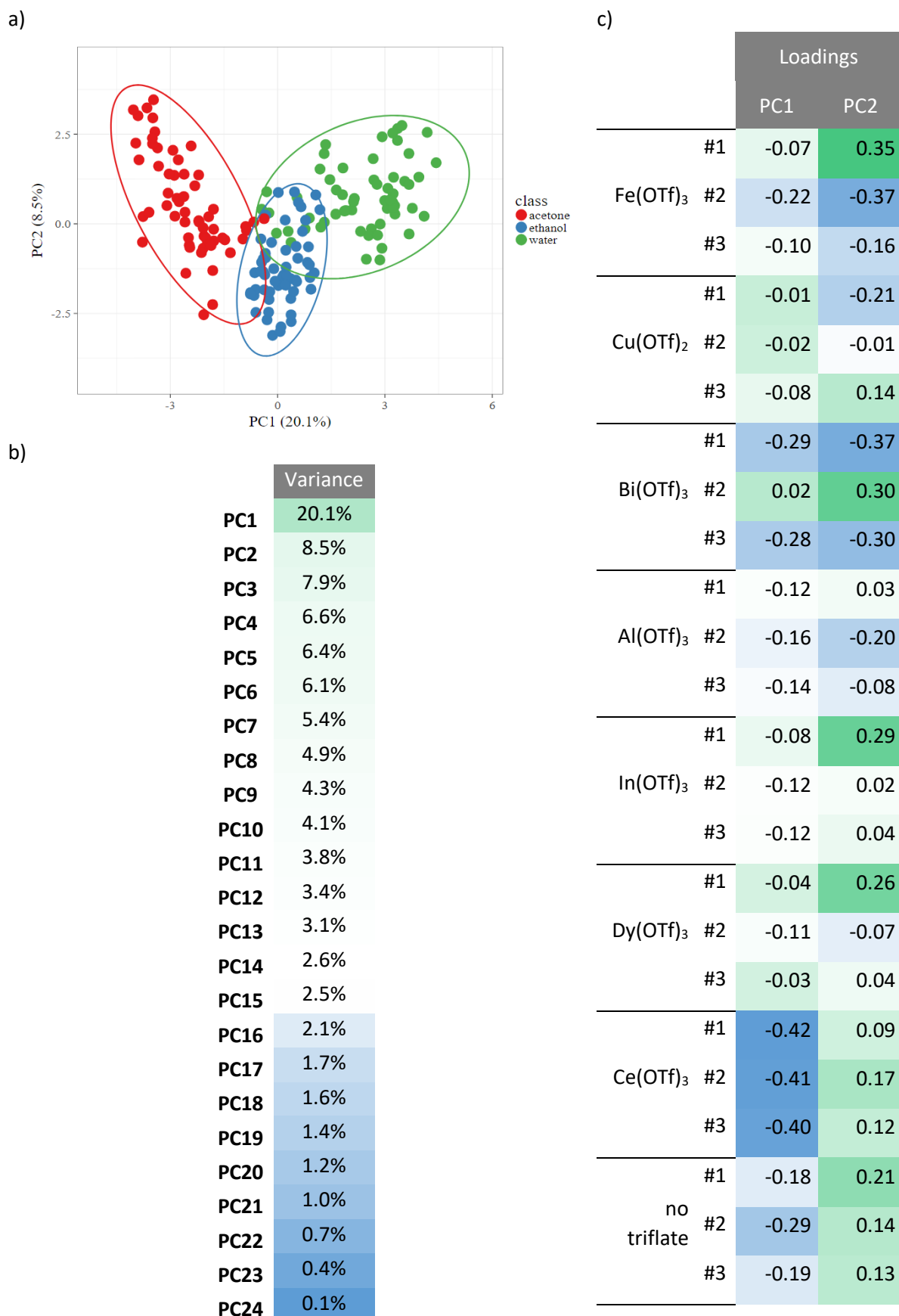


Figure S32. PCA on α_2 , for R is measured at different time interval [130s;139s] | a, PCA scores with 95% confidence ellipsoids. b, Individual variance for the different PC. c, PCA loadings of the different sensing elements' response for PC1 and PC2.

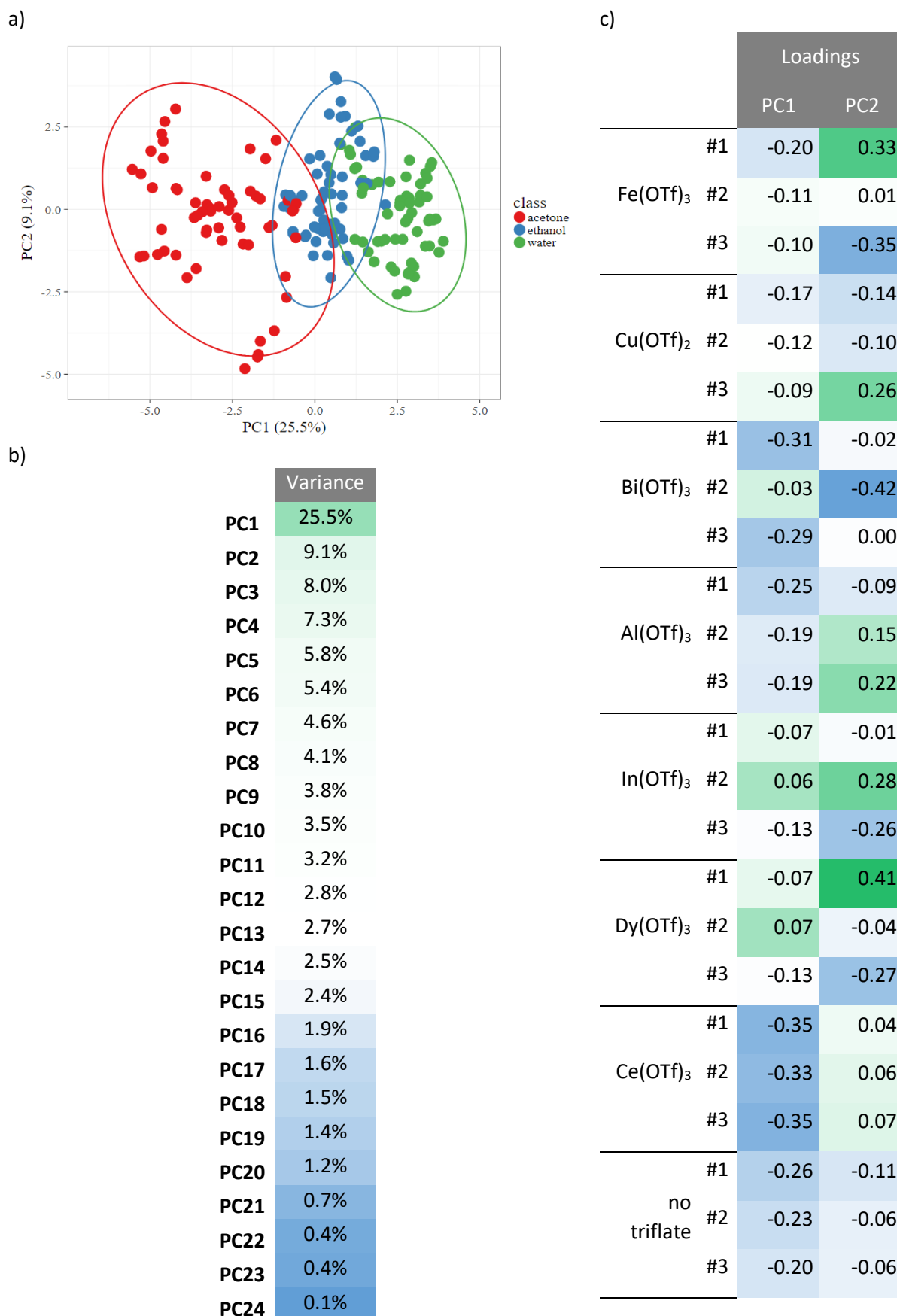


Figure S33. PCA on α_2 , for R is measured at different time interval [140s;149s] | a, PCA scores with 95% confidence ellipsoids. b, Individual variance for the different PC. c, PCA loadings of the different sensing elements' response for PC1 and PC2.

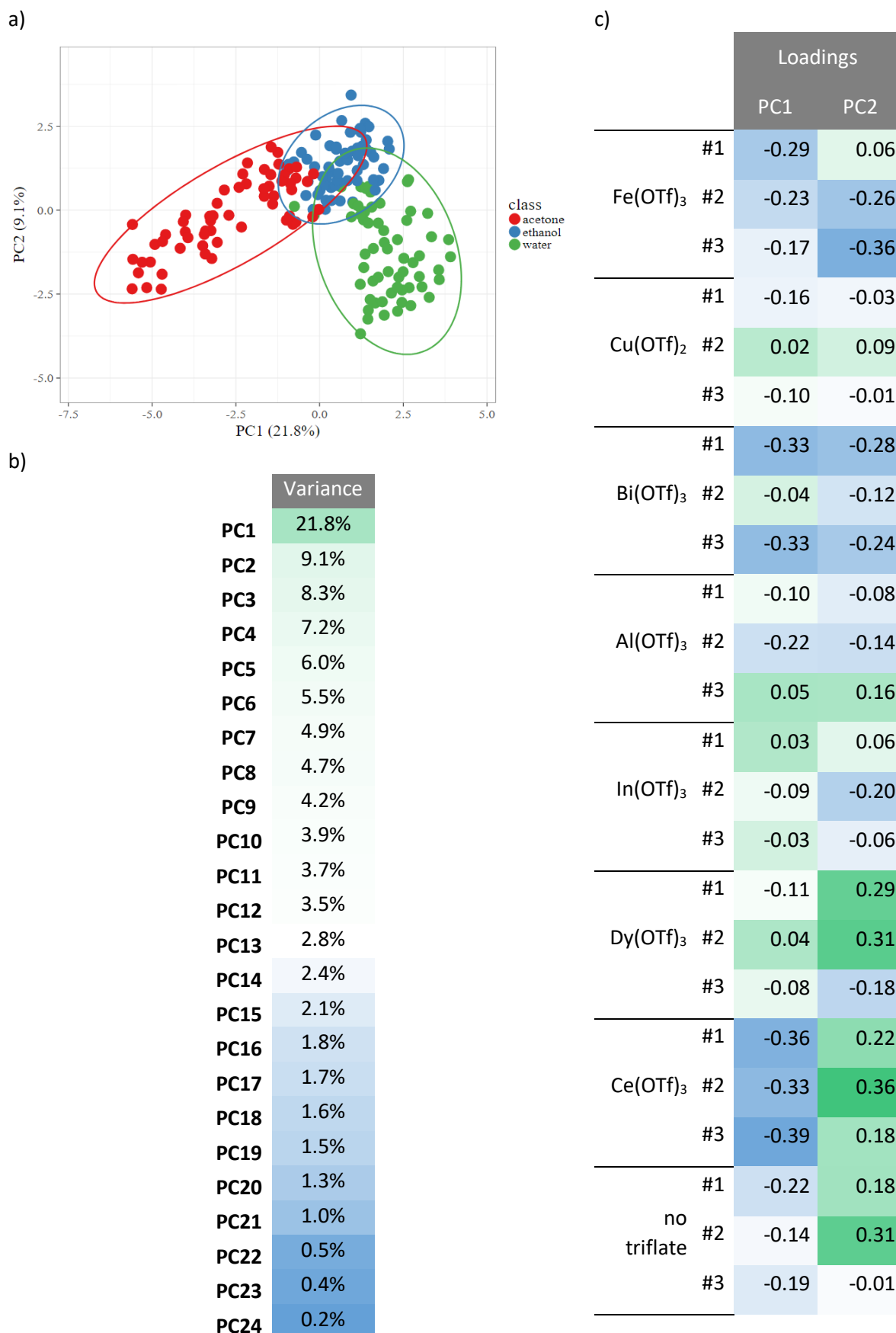
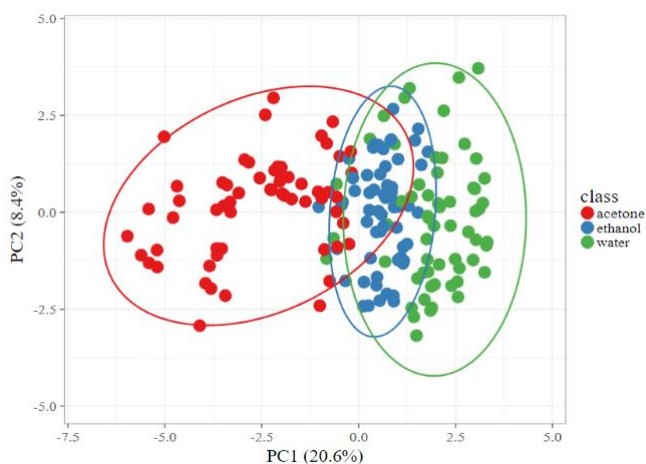


Figure S34. PCA on α_2 , for R is measured at different time interval [150s;159s] | a, PCA scores with 95% confidence ellipsoids. b, Individual variance for the different PC. c, PCA loadings of the different sensing elements' response for PC1 and PC2.

a)



b)

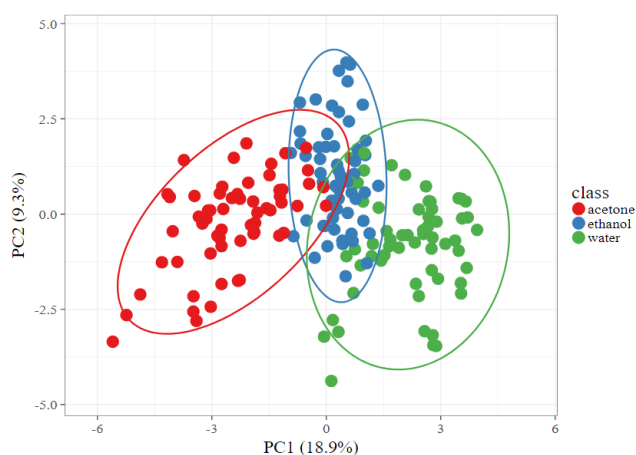
	Variance
PC1	20.6%
PC2	8.4%
PC3	8.2%
PC4	7.0%
PC5	6.0%
PC6	5.4%
PC7	5.2%
PC8	5.0%
PC9	4.3%
PC10	3.8%
PC11	3.5%
PC12	3.1%
PC13	3.0%
PC14	2.6%
PC15	2.3%
PC16	2.2%
PC17	2.1%
PC18	1.8%
PC19	1.6%
PC20	1.4%
PC21	1.2%
PC22	0.6%
PC23	0.4%
PC24	0.3%

c)

		Loadings	
		PC1	PC2
Fe(OTf) ₃	#1	0.18	-0.21
	#2	0.16	0.14
	#3	0.23	0.30
Cu(OTf) ₂	#1	0.08	0.34
	#2	-0.09	-0.30
	#3	0.13	-0.07
Bi(OTf) ₃	#1	0.34	0.01
	#2	0.09	0.12
	#3	0.30	-0.08
Al(OTf) ₃	#1	0.10	-0.32
	#2	0.17	-0.16
	#3	0.15	0.18
In(OTf) ₃	#1	0.08	-0.04
	#2	0.08	-0.40
	#3	0.13	-0.07
Dy(OTf) ₃	#1	0.07	-0.04
	#2	0.06	-0.20
	#3	-0.02	-0.20
Ce(OTf) ₃	#1	0.39	-0.06
	#2	0.38	-0.14
	#3	0.39	-0.10
no triflate	#1	0.17	0.01
	#2	0.20	0.37
	#3	0.18	0.19

Figure S35. PCA on α_2 , for R is measured at different time interval [160s;169s] | a, PCA scores with 95% confidence ellipsoids. b, Individual variance for the different PC. c, PCA loadings of the different sensing elements' response for PC1 and PC2.

a)



b)

	Variance
PC1	18.9%
PC2	9.3%
PC3	8.0%
PC4	6.8%
PC5	6.6%
PC6	6.0%
PC7	5.2%
PC8	5.1%
PC9	4.3%
PC10	4.1%
PC11	3.9%
PC12	3.3%
PC13	3.1%
PC14	2.6%
PC15	2.2%
PC16	2.0%
PC17	1.8%
PC18	1.7%
PC19	1.4%
PC20	1.2%
PC21	1.0%
PC22	0.6%
PC23	0.5%
PC24	0.3%

c)

		Loadings	
		PC1	PC2
Fe(OTf) ₃	#1	-0.20	-0.06
	#2	-0.10	0.40
	#3	-0.17	0.16
Cu(OTf) ₂	#1	-0.12	0.33
	#2	-0.07	-0.11
	#3	-0.11	0.02
Bi(OTf) ₃	#1	-0.33	-0.18
	#2	-0.18	-0.32
	#3	-0.35	-0.12
Al(OTf) ₃	#1	-0.03	-0.13
	#2	-0.06	-0.28
	#3	-0.11	-0.32
In(OTf) ₃	#1	0.03	0.27
	#2	-0.10	0.00
	#3	0.01	-0.33
Dy(OTf) ₃	#1	-0.14	0.09
	#2	-0.14	0.02
	#3	0.07	0.02
Ce(OTf) ₃	#1	-0.42	0.02
	#2	-0.42	0.11
	#3	-0.40	0.00
no triflate	#1	-0.04	-0.15
	#2	-0.06	0.08
	#3	-0.18	0.34

Figure S36. PCA on α_2 , for R is measured at different time interval [170s;179s] | a, PCA scores with 95% confidence ellipsoids. b, Individual variance for the different PC. c, PCA loadings of the different sensing elements' response for PC1 and PC2.